



A nonmagnetic differentiated early planetary body



Benjamin P. Weiss^{a,*}, Huapei Wang^a, Thomas G. Sharp^b, Jérôme Gattacceca^c,
David L. Shuster^{d,e}, Brynna Downey^a, Jinping Hu^b, Roger R. Fu^a, Aaron T. Kuan^f,
Clément Suavet^a, Anthony J. Irving^g, Jun Wang^h, Jiajun Wang^h

^a Department of Earth, Atmospheric, and Planetary Sciences, Massachusetts Institute of Technology, 77 Massachusetts Avenue, Cambridge, MA 02139, USA

^b School of Earth and Space Exploration, Arizona State University, Tempe, AZ, USA

^c Centre National de la Recherche Scientifique, Aix-Marseille Université, Institut de Recherche pour le Développement, Collège de France, CEREGE, Aix-en-Provence, France

^d Department of Earth and Planetary Science, University of California, Berkeley, CA 94720, USA

^e Berkeley Geochronology Center, 2455 Ridge Road, Berkeley, CA 94709, USA

^f Department of Neurobiology, Harvard Medical School, Boston, MA 02115, USA

^g Department of Earth and Space Sciences, University of Washington, Seattle, WA 98195, USA

^h National Synchrotron Light Source-II, Brookhaven National Laboratory, Upton, NY 11973, USA

ARTICLE INFO

Article history:

Received 19 November 2016

Received in revised form 21 February 2017

Accepted 22 March 2017

Available online 19 April 2017

Editor: B. Buffett

Keywords:

planetesimals
paleomagnetism
meteorites
dynamo
differentiation

ABSTRACT

Paleomagnetic studies of meteorites have shown that the solar nebula was likely magnetized and that many early planetary bodies generated dynamo magnetic fields in their advecting metallic cores. The surface fields on these bodies were recorded by a diversity of chondrites and achondrites, ranging in intensity from several μT to several hundred μT . In fact, an achondrite parent body without evidence for paleomagnetic fields has yet to be confidently identified, hinting that early solar system field generation and the dynamo process in particular may have been common. Here we present paleomagnetic measurements of the ungrouped achondrite NWA 7325 indicating that it last cooled in a near-zero field ($< \sim 1.7 \mu\text{T}$), estimated to have occurred at 4563.09 ± 0.26 million years ago (Ma) from Al–Mg chronometry. Because NWA 7325 is highly depleted in siderophile elements, its parent body nevertheless underwent large-scale metal-silicate differentiation and likely formed a metallic core. This makes NWA 7325 the first recognized example of an essentially unmagnetized igneous rock from a differentiated early solar system body. These results indicate that all magnetic fields, including those from any core dynamo on the NWA 7325 parent body, the solar nebula, young Sun, and solar wind, were $< 1.7 \mu\text{T}$ at the location of NWA 7325 at 4563 Ma. This supports a recent conclusion that the solar nebula had dissipated by ~ 4 million years after solar system formation. NWA 7325 also serves as an experimental control that gives greater confidence in the positive identification of remanent magnetization in other achondrites.

© 2017 Elsevier B.V. All rights reserved.

1. Introduction

The existence of dozens of achondrite groups and ungrouped achondrites indicates that numerous planetesimals experienced large-scale melting and differentiation in the early solar system (Scheinberg et al., 2015b). Much of the energy for melting was likely supplied by the decay of the short-lived radionuclide ^{26}Al , which should have substantially heated bodies that accreted a large fraction of their masses within 2 million years (My) after the formation of calcium aluminum-rich inclusions (CAIs) (Weisberg et al., 2006). Hf–W chronometry of iron meteorites confirms that

many bodies experienced large-scale metal-silicate fractionation during this period (Kruijer et al., 2014). Thermal and compositional core convection (Nimmo, 2009), possibly combined with mechanical stirring from impacts, likely powered core advection for ten to perhaps a few hundred My (Bryson et al., 2015; Elkins-Tanton et al., 2011; Formisano et al., 2016; Scheinberg et al., 2015a; Sterenberg and Crowley, 2013).

Scaling relationships derived from magnetohydrodynamic simulations of convecting metallic cores indicate that many of these bodies should have been capable of generating dynamos (Weiss et al., 2010). Indeed, essentially every achondrite group that has yet been studied with modern paleomagnetic methods has been found to contain ancient natural remanent magnetization (NRM): evidence for past core dynamos has been identified in plutonic angrites (Wang et al., 2017), eucrites (Fu et al., 2012), and main

* Corresponding author. Fax: +617 258 7401.

E-mail address: bpweiss@mit.edu (B.P. Weiss).

group pallasites (Bryson et al., 2015; Tarduno et al., 2012). Remanent magnetization attributed to possible core dynamos has even been found in CV (Carporzen et al., 2011; Gattacceca et al., 2016) and CM chondrites (Cournède et al., 2015). Although a study of five eucrites including ALHA81001 and PCA 82502 concluded that they recorded low-field (<10 μ T) conditions (Cisowski, 1991), this study lacked precise radiometric ages and thermochronometry, used only relatively low-field alternating field (AF) demagnetization, and was unable to prevent thermochemical alteration of the samples during thermal demagnetization; recent studies of ALHA81001 and PCA 82502 identified stable, unidirectional NRM of extraterrestrial origin acquired in fields of ~ 12 and ~ 70 μ T, respectively (Fischer et al., 2013; Fu et al., 2012). All told, the available paleomagnetic data indicate that planetesimal dynamos were likely common, if not ubiquitous, in the early solar system.

Nevertheless, it is expected that not all differentiated bodies that underwent large-scale metal-silicate fractionation should have been capable of generating dynamos. There are numerous reasons a dynamo might be inhibited on a differentiated body. First, it is possible that a body underwent large-scale metal-silicate fractionation but formed localized, dispersed metal-rich regions rather than a large metallic core. The low gravity and possibility of incomplete melting on planetesimals means that even if temperatures exceeded that of the Fe–S solidus, metal percolation to the center of planetesimals was not guaranteed (Cerantola et al., 2015). Possible examples of such bodies include the winonaite-IAB iron meteorite parent body and the IIE iron meteorite parent body (Ruzicka, 2014). Second, even if a metallic core formed, it may have not advected. Thermal convection would be inhibited by sufficiently slow cooling rates, as might be expected if the overlying mantle was solid and sufficiently thick; such an outcome may be consistent with the proposal that planetesimals never formed silicate magma oceans but only melted episodically and in small quantities (Wilson and Keil, 2012). Compositional convection is a potent power source but is only expected for metallic cores containing a light alloying element (Nimmo, 2009). Furthermore, although both outward core crystallization and inward core crystallization in the iron snow regime (Rückriemen et al., 2015) provide a buoyancy flux for driving convection, inward dendritic core crystallization does not (Scheinberg et al., 2015a). Third, even if the metallic core advected, it still might not generate a dynamo. Fluid velocities may be too slow, as expected for core radii smaller than ~ 80 – 100 km (Elkins-Tanton et al., 2011; Nimmo, 2009; Weiss et al., 2010) or perhaps even ranging up to radii of 1000 km (Sternberg and Crowley, 2013), or the velocity field may have an unsuitable geometry (e.g., not lead to a field-amplification instability) (Stevenson, 1983). One or more of these reasons can account for why, among all rocky and icy solar system bodies, only the Earth, Mercury, and Ganymede are known to have active dynamos today (Stevenson, 2010). Finally, even if a body generated a dynamo, meteorites from this body may not retain records of this field if the meteorites were last cooled or aqueously altered when the dynamo was not active. In particular, it has recently been argued that thermal blanketing of planetesimal cores by ^{26}Al -enriched mantles should delay thermal convection dynamos until at least several million years after differentiation (Sternberg and Crowley, 2013).

We see that there is every expectation that differentiated planetesimals should have formed in the early solar system that either never generated magnetic fields or at least produced fields not recorded by achondrites from these bodies. Searching for such examples would not only establish the frequency and diversity of planetesimal dynamo activity, but also test the methodologies that have been developed for identifying dynamos from the meteorite record. In short, demonstrating our ability to identify unmagnetized meteorites would build greater confidence in our identifica-

tion of magnetized meteorites. Additionally, identification of unmagnetized meteorites would enable constraints on the intensity of magnetic fields generated external to their parent bodies like, those from the solar nebula and early solar wind.

Because arbitrarily weak paleofields will produce essentially no detectable NRM, it is not possible to demonstrate that an apparently unmagnetized rock formed in truly zero-field conditions but only to place an upper limit on the paleofield. Even so, meteorites with near-zero paleointensities are difficult to identify because they are unfamiliar: essentially all Earth rocks that have been studied with paleomagnetic methods formed in the geomagnetic field. Furthermore, numerous processes can impart secondary magnetization after the meteorites arrive at Earth and enter the geomagnetic field: surficial heating during atmospheric entry, weathering and associated crystallization of ferromagnetic grains, viscous remanence acquisition, and application of hand magnets by meteorite collectors (Weiss et al., 2010). Another major problem is the acquisition of spurious remanence during the laboratory demagnetization process. The ferromagnetism of the vast majority of basaltic achondrites is dominated by the iron–nickel minerals kamacite and martensite, which usually form low-coercivity, multidomain grains that readily acquire spurious remanence during alternating field (AF) demagnetization (Weiss et al., 2010). This spurious remanence could potentially be mistaken for NRM or, at the very least, limits out ability to put stringent upper limits on the paleointensities for these samples. Furthermore, thermal demagnetization of these samples typically leads to thermochemical alteration of these iron–nickel minerals (Suavet et al., 2014), which can render paleointensities measured using laboratory heating methods inaccurate. Finally, because individual ferromagnetic grains have spontaneous magnetization even when the bulk rock is not magnetized, paleomagnetic analysis of small samples (as is common in extraterrestrial paleomagnetic studies) is fundamentally limited by the statistics of small numbers of grains (Berndt et al., 2016; Lima and Weiss, 2016). As a result of these limitations, only recently have we been able to confidently identify largely unmagnetized rocks from the Moon that place meaningful upper limits (<4 μ T) on the paleofield after 3.5 Ga (Tikoo et al., 2014).

Identification of null magnetic field conditions on an early planetesimal requires an ancient, well-preserved sample with high-fidelity magnetic recording properties. Here we present paleomagnetic, petrographic, and $^{40}\text{Ar}/^{39}\text{Ar}$ analyses of the ungrouped basaltic achondrite Northwest Africa (NWA) 7325. Our measurements show that this meteorite was last cooled from above the peak magnetic disordering temperature ($\sim 780^\circ\text{C}$) in a field of no greater than ~ 1.7 μ T.

2. Petrology, thermal history, and age of NWA 7325

NWA 7325 is a dark green achondrite partially covered with a chartreuse-colored fusion crust found as 37 separate pieces in southern Morocco in 2012 (Barrat et al., 2015; Irving et al., 2013). It is an unbrecciated, fine- to medium-grained (typical grain size 0.5 – 1 mm) plutonic rock (probably a cumulate) composed of 56 vol.% calcic plagioclase, 27 vol.% diopside, 16 vol.% forsterite and accessory troilite containing Cr-rich lamellae, chromite, and FeNi metal.

NWA 7325 is thought to have been produced as a partial melt in the rocky exterior of a highly differentiated parent body (Barrat et al., 2015; Weber et al., 2016). Its abundances of highly siderophile elements are depleted by 3–4 orders of magnitude relative to CI chondrites, suggesting that its parent body underwent large-scale metal-silicate fraction (Archer et al., 2015). NWA 7325's distinctive elemental composition and unique combination of O and ^{54}Cr isotopes (Barrat et al., 2015; Irving et al., 2013) indicate

that it is derived from a parent body not sampled by other achondrites. It has even been suggested that this parent body could be Mercury (Irving et al., 2013; Koefoed et al., 2016).

With a pyroxene Pb–Pb age of 4563.4 ± 2.6 Ma, an Al–Mg model age of 4563.09 ± 0.26 Ma (Koefoed et al., 2016) and a I–Xe model age of 4563.4 ± 0.26 Ma (Gilmour and Crowther, 2017) NWA 7325 has one of the oldest crystallization ages amongst known igneous rocks. Although cracks in the meteorite contain secondary carbonate from terrestrial weathering and very rare secondary oxides (Barrat et al., 2015; Weber et al., 2016), NWA 7325 is overall very fresh and nearly all metal grains are unaltered. Nevertheless, multiple lines of evidence suggest that following its formation, NWA 7325 was substantially reheated and partially melted, followed by rapid cooling. Olivines in the meteorite exhibit undulatory extinction and fracturing while plagioclase is not maskelytinized, suggesting the meteorite experienced shock pressures of 5–10 GPa (shock stage 2) (Weber et al., 2016). Despite these relatively low shock pressures, there is abundant evidence for a brief high-temperature event that led to localized melting. A second generation of fine (<20 μm) plagioclase laths crystallized in cracks and at grain boundaries with mafic minerals, in some cases in contact with SiO_2 -normative late-stage melts (Weber et al., 2016). Furthermore, plagioclase contains finely dispersed tiny (<5 μm) metal and iron sulfide grains, suggesting it was melted and then cooled rapidly (Weber et al., 2016) (Fig. 1A, D–E). As described in Section 3.1, our observations of partial desulfurization of FeS provide additional evidence for this remelting event. ^{26}Al (Barrat et al., 2015) and ^{129}Xe (Weber et al., 2016; Gilmour and Crowther, 2017) isotopic data are consistent with this melting event occurring just ~ 4 My after the formation of CAIs. Such an early age for this thermal event is also consistent with bulk rock and plagioclase $^{40}\text{Ar}/^{39}\text{Ar}$ ages of 4516 ± 160 Ma and 4481 ± 150 Ma (Weber et al., 2016).

In an attempt to further constrain the age and thermal history of NWA 7325, we conducted $^{40}\text{Ar}/^{39}\text{Ar}$ stepwise degassing analysis of a neutron-irradiated bulk chip from the meteorite (Fig. S1). As described in the supplementary text, this experiment was not successful due to a lack of statistical concordance of the results.

3. Ferromagnetic grains

3.1. Mineralogy

To determine the mineralogy and constrain the grain size and setting of the ferromagnetic minerals in NWA 7325, we conducted backscattered electron microscopy (BSEM), electron dispersive spectroscopy (EDS), and transmission electron microscopy (TEM) analyses in the MIT Experimental Petrography Lab, Harvard Center for Nanoscale Science, and LeRoy Eyring Center for Solid State Science at Arizona State University. These data collectively confirm the presence of numerous fine (mostly <1 μm size, with many grains <0.1 μm) metal and Cr-rich iron sulfide grains showing few secondary alteration textures (Figs. 1 and S2 and Table S2). Wavelength dispersive spectroscopy (WDS) showed that nearly all metal grains are FeNi metal (87–92% Fe alloyed with 5–10% Ni), although we observed one large Cr-rich FeNi grain (Table S2 and Fig. 1B). Multiple WDS analyses taken from within single metal grains did not detect significant variations in Ni abundances, while our high-contrast BSEM and bright-field TEM images show no evidence of exsolution textures in the metal grains down to the resolution of the images (~ 0.1 μm and <10 nm, respectively). Therefore, the metal grains' Ni-abundance indicates that they should be dominantly in the form of the body-centered cubic (bcc) phase martensite (α_2 -FeNi). Electron diffraction patterns from the FeNi grains confirm a bcc structure (Fig. 1F–G). The presence of lamellar twins and evidence for lattice strain in some of these metal

particles (Fig. 1H) are consistent the presence of lath martensite, the expected martensite morphology for the low-Ni, low-C composition of the metal in NWA 7325 that crystallized from the parent γ -FeNi (fcc) phase (Krauss, 2005). The host for the metal particles is polycrystalline plagioclase, consisting of nanocrystals with an apparent lattice-preferred orientation (Fig. 1F). The metal particles are closely associated with FeS grains and voids in the plagioclase (Fig. 1E–F). This association suggests that the metal formed by the partial desulfidization of the FeS, producing metal and sulfur vapor, providing more evidence for a second melting event after formation of the rock (see Section 2.1).

Our rock magnetic experiments provide further evidence that martensite is the dominant ferromagnetic mineral and additionally constrain its domain size and coercivity. Martensite with the composition found in NWA 7325 should have martensite-start and martensite-finish temperatures ranging between 680–510 °C and 630–430 °C, respectively, and austenite-start and austenite-finish temperatures of 760–680 °C and 780–700 °C, respectively (Swartzendruber et al., 1991). These temperatures are consistent with our thermomagnetic measurements (Fig. 2), which show hysteretic behavior indicative of sluggish transformations from α_2 -FeNi to γ -FeNi occurring at 760–800 °C during warming and γ -FeNi to α_2 -FeNi at ~ 550 –560 °C during cooling. Our measurements of saturation magnetization, M_s , of subsamples SR1 and JG2 of NWA 7325 indicate a metal abundance of 243 and 358 ppm by mass [assuming a M_s for pure Fe of $224 \text{ Am}^2 \text{ kg}^{-1}$ (Dunlop and Özdemir, 1997)].

Low-temperature cycling of room-temperature saturation remanence, M_{rs} , using a Quantum Designs Magnetic Properties Measurement System at the Institute for Rock Magnetism identified a weak magnetic transition at a temperature of ~ 118 K, consistent with the Verwey transition of magnetite [although no Verwey transition was detectable in a field cooled warming of low temperature M_{rs} experiment] (Fig. S3). Given the small observed saturation remanence decrease (average of $2.85 \times 10^{-5} \text{ Am}^2 \text{ kg}^{-1}$ across the Verwey transition temperature for two repeat field-cooled warming experiments), magnetite's M_s of $92 \text{ Am}^2 \text{ kg}^{-1}$, assuming the magnetite grains are pseudo single domain (PSD) in size and so have $M_{rs}/M_s \sim 0.1$, and assuming demagnetization of magnetite's M_{rs} by 50% across the Verwey transition (Özdemir et al., 2002), this indicates that NWA 7325 contains just ~ 6 ppm magnetite by mass, consistent with petrographic evidence for very minor terrestrial weathering (see above).

3.2. Thermochemical stability of magnetization carriers

The valence states of Cr, V, and Ti in NWA 7325 indicate the meteorite formed under highly reducing conditions with an estimated oxygen fugacity somewhere between 2 and 7 log units below the iron–wüstite (IW) buffer (Sutton et al., 2014). As a result, we conducted our thermal demagnetization and paleointensity analyses (Sections 4 and 5) under controlled oxygen fugacity conditions to mitigate thermochemical alteration of the ferromagnetic grains. However, because of the large range in oxygen fugacity estimates for NWA 7325, we first heated subsamples of the meteorite under a range of reducing conditions and temperatures to establish the optimal oxygen fugacity for mitigating alteration of the rock magnetic properties. These experiments were conducted in a thermal demagnetization system that employs regulated CO_2 – H_2 gas mixing (Suavet et al., 2014).

Prior to each heating step, we conducted repeated rock magnetic experiments to quantify the effect of subsequent heating on the magnetization carrying-capacity of the rock. Beginning with fresh unheated samples, we measured anhysteretic remanent magnetization (ARM) acquisition in a peak alternating field (AF) of 200 mT and bias fields ranging from 0.05 to 1.5 mT, AF demag-

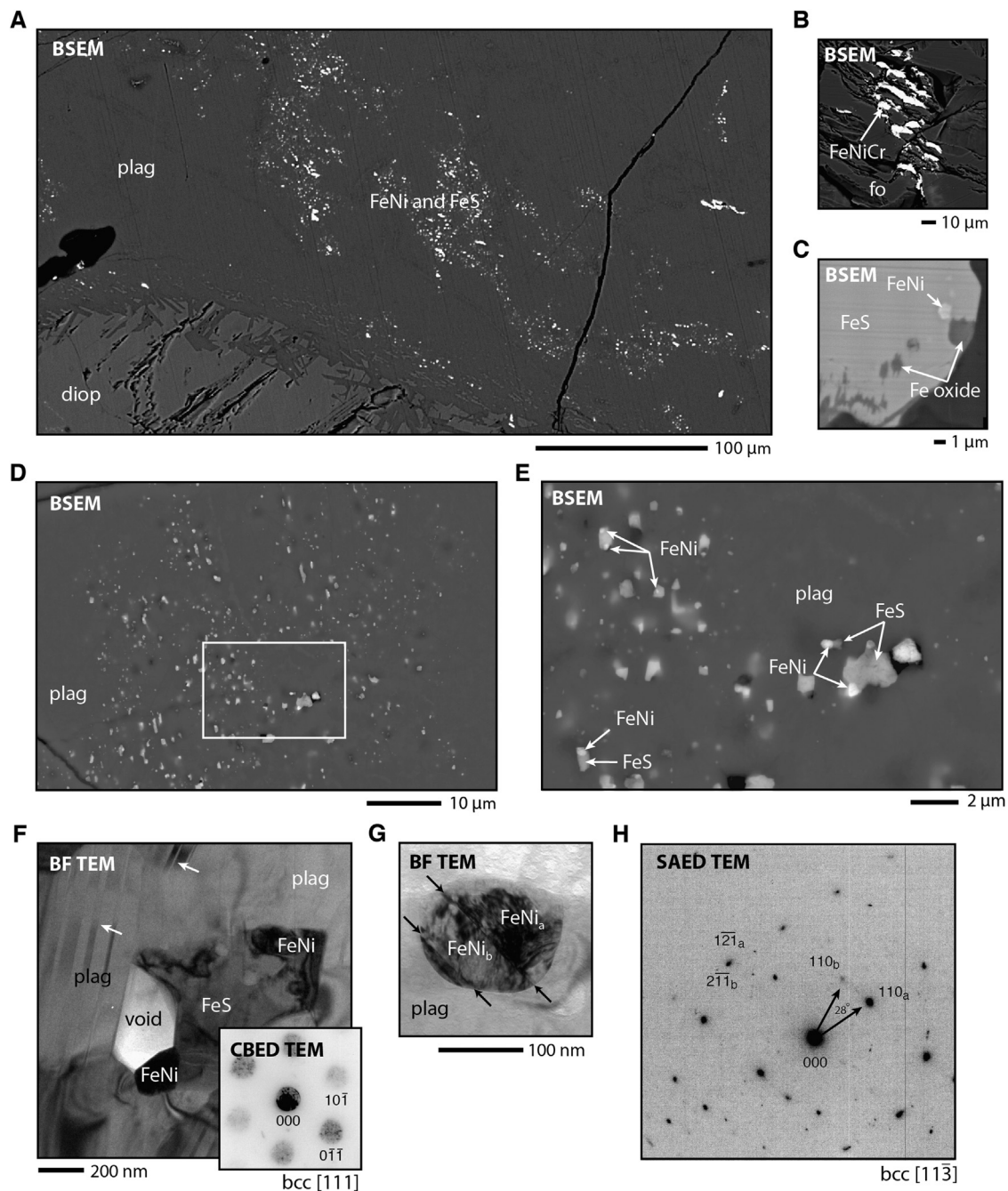


Fig. 1. Electron microscopy analyses of NWA 7325. (A) Overview BSEM image showing dominant occurrence of FeNi and FeS grains as submicrometer inclusions in plagioclase (plag). Plagioclase commonly exhibits reaction relationships with adjacent diopside (diop), suggestive of a partial remelting event after formation. (B) BSEM image of rare CrFeNi metal grains. (C) BSEM image of rare secondary Fe oxide metal grains associated with an FeNi–FeS assemblage. (D) BSEM image showing plagioclase (dark gray) with disseminated particles of Fe–Ni metal (white) and troilite (FeS; light gray). The metal and sulfide phases form intergrown assemblages with diameters ranging from tens of nanometers to several micrometers. (E) Higher magnification BSEM image of boxed region in (D) showing composite FeS and FeNi particles in plagioclase with associated voids (dark zones adjacent to some metal and sulfide particles). (F) Bright-field (BF) TEM image of an FeS crystal (medium grey) in contact with two FeNi particles (dark grey) and a void (lightest grey) within a polycrystalline aggregate of anorthitic plagioclase (plag). Albite twins in the anorthite are visible as bands of alternating diffraction contrast (arrows). The inset convergent-beam electron diffraction (CBED) pattern, from the lower FeNi particle, is indexed as a $\langle 111 \rangle$ zone axis pattern for body-centered cubic ($Im\bar{3}m$) α -FeNi. The mottled contrast visible in the central beam and diffraction spots of the CBED pattern illustrate local lattice strain within the FeNi crystal. (G) BF TEM image of an FeNi particle showing a lamellar twin bounded by planar twin boundaries (arrows). The FeNi_a twin domain (dark) is imaged along the $[11\bar{3}]$ zone axis and the FeNi_b domain is imaged nearly along $[11\bar{3}]$. Local variations in diffraction contrast within the twin domains indicate local lattice strain associated with a high density of defects. (H) Selected area electron diffraction (SAED) pattern of the twinned crystal shown in (G). The pattern consists of two $[11\bar{3}]$ zone axis patterns related by a $\sim 28^\circ$ rotation about $[11\bar{3}]$. The patterns were collected with domain FeNi_a aligned along $[11\bar{3}]$ and domain FeNi_b slightly off $[11\bar{3}]$. As shown in Fig. S2, this twin relationship is consistent with the martensitic phase transition from γ -FeNi (fcc) to α_2 -FeNi (bcc).

netized this ARM to 400 mT, conducted stepwise IRM acquisition up to 1 T, and finally AF demagnetized this IRM to 400 mT. We then gave the samples another IRM in a 1 T field and then heated them to a particular temperature in zero field. We then AF demagnetized this partially thermally demagnetized IRM and again

measured stepwise IRM acquisition up to 1 T. This sequence of measurements was then repeated for increasingly higher heating temperatures ranging up to 600 °C and in oxygen fugacity conditions ranging from IW to well below IW-4 [the most reducing experiments employed essentially pure (99.995%) lab-grade H₂ gas].

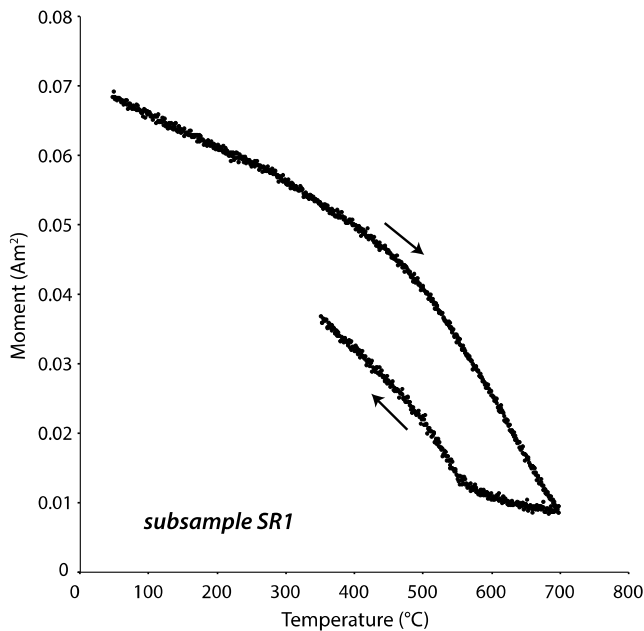


Fig. 2. Saturation magnetization of NWA 7325 subsample SR1 as a function of temperature during heating up to 800 °C and cooling down to 350 °C. Fitting the warming data over the interval of 400–750 °C with the extrapolation method of Moskowitz (1981) yields a mean austenite-finish temperature (i.e., martensite-to-austenite transition temperature) of 762–796 °C. Although this method is designed to quantify Curie temperatures, it should give an accurate estimate of the austenite-finish temperature because the latter is very close to martensite's 780 °C Curie temperature. These data were acquired on fresh (unheated) subsample SR1 following all other rock magnetic measurements on this subsample (Figs. 4 and S2).

The results show that under all oxygen fugacity conditions studied, thermochemical alteration of the magnetic carriers, manifested as strong increases in magnetization intensity, occurred after temperatures reached 400 °C, at which point ARM and IRM reached values ~ 3 times that of the original unheated sample (although one subsample heated under IW-3 conditions, 7B3B, remained relatively unaltered up to at least 500 °C) (Fig. S4). The condition that resulted in the least alteration at 300 °C was IW-3 (for which ARM and IRM increased by several tens of %), although IW-2 and IW conditions yielded very similar results. Even so, after heating in IW-3 conditions to 500 °C and 800 °C, ARM and IRM increased by

factors of ~ 2 –6 and ~ 7 –10, respectively. Our inability to mitigate alteration may reflect the fact NWA 7325 cooled under temporally-varying oxygen fugacity conditions; this possibility is consistent with the 5 orders of magnitude range in oxygen fugacity estimates for the meteorite (Sutton et al., 2014). Another likely problem is that we did not control for sulfur fugacity despite the presence of sulfides in the meteorite.

3.3. Grain size and habit

Determining the domain size and habit of ferromagnetic grains is important for establishing whether the grains can retain high-fidelity records of ancient magnetic fields and also for calibrating our non-thermal paleointensity analyses (Section 5.2). As discussed in Section 3.1, our BSEM and TEM images observed FeNi grains with sizes mainly ranging from 0.1 to 1 μm . This range indicates a dominantly PSD size range (Einsle et al., 2016). To obtain additional information on the domain size and habit of the FeNi grains, we conducted X-ray tomography and hysteresis measurements.

To image the three dimensional sizes and shapes of the larger FeNi grains, we conducted synchrotron-based full-field transmission hard X-ray microscopy (TXM) using a recently developed transmission hard X-ray microscope at beamline X8C at the National Synchrotron Light Source (NSLS), Brookhaven National Laboratory (BNL) (Wang et al., 2012). TXM has the advantage over TEM of enabling three dimensional analyses over much larger fields of view. We mounted a mm-sized grain from of NWA 7325 on a tungsten carbide pin, which was then placed on a kinematic stage. To target the FeNi minerals, we used an X-ray energy of 7.2 keV, just above the Fe absorption K-edge (7.112 keV) (Baker et al., 2012). We acquired images each with a field-of-view of 40 $\mu\text{m} \times 40 \mu\text{m}$ and an effective pixel size of 40 nm after using 2×2 pixel binning. We then stitched together the TXM images to construct a 240 \times 240 μm image (Fig. 3A). We then rotated the sample 90° and conducted the same X-ray imaging for a side view (Fig. 3B). For a 40 μm cylindrical volume near the tip of the sample, we also conducted tomographic scans by taking 721 single X-ray images every 0.25° from 0° to 180°, which were then used reconstruct a three-dimensional rendering of the cylinder (Movie S1). These X-ray data confirm the existence of abundant $<1 \mu\text{m}$ sized iron mineral grains with similar sizes as those visible in the SEM images (Fig. 3C and D).

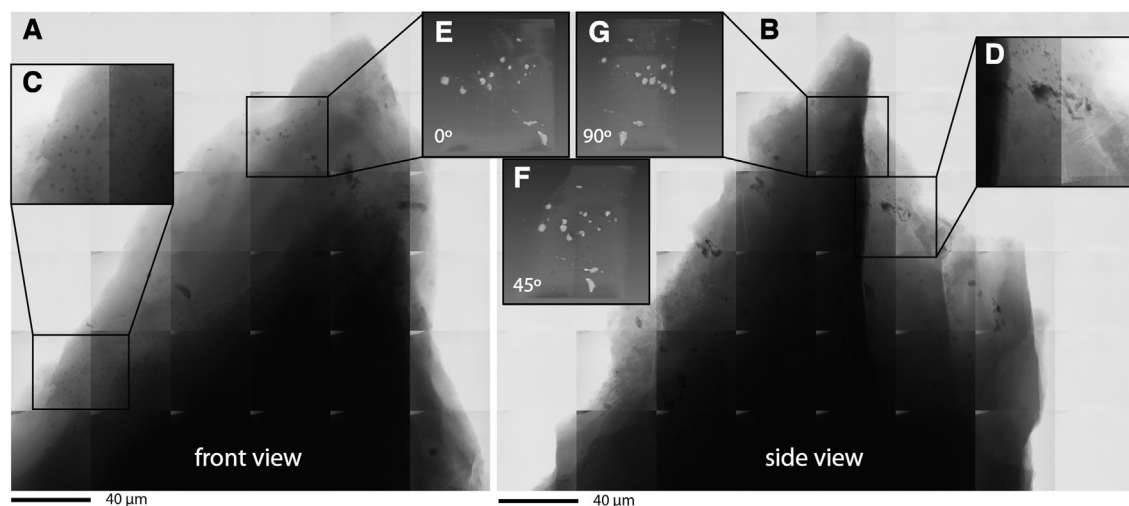


Fig. 3. TXM imaging of NWA 7325. (A) Mosaic TXM image of a silicate grain from NWA 7325 stitched from 40 $\mu\text{m} \times 40 \mu\text{m}$ images (2×2 pixel binning), front view. (B) Side view of the same NWA 7325 grain. (C, D) Zoom-in to areas containing fine iron-bearing particles. (E–G) Selected frames (0°, 45°, and 90°) from the tomographic three-dimensional reconstruction movie (Movie S1) of a 40 μm cylindrical volume of NWA 7325. In (A)–(D), higher concentrations of iron are darker, whereas in (E) to (G), higher concentrations of iron are brighter.

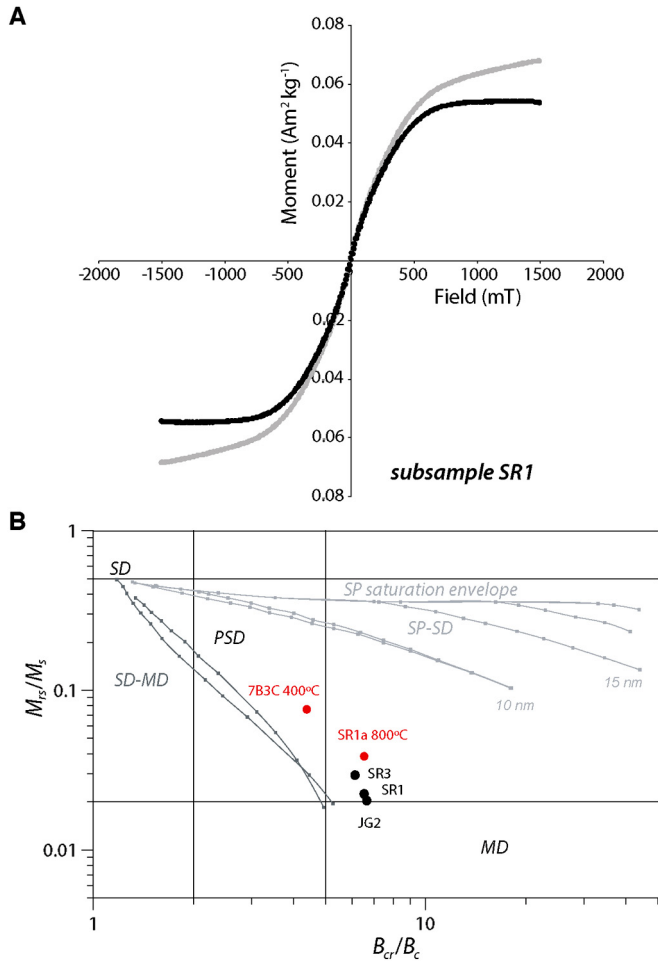


Fig. 4. Hysteresis properties of NWA 7325. (A) Room temperature hysteresis loop measured for fresh NWA 7325 subsample SR1. Shown is sample moment as a function of applied field. The black curve represents the hysteresis loop after subtraction of paramagnetic and diamagnetic contributions. The gray curve represents the raw (uncorrected) data. (B) Dunlop-Day plot (Dunlop, 2002) showing the ratio of coercivity of remanence to coercivity (B_{cr}/B_c) versus the ratio of saturation remanence to saturation magnetization (M_{rs}/M_s) for NWA 7325 subsamples. Single domain (SD), pseudo single domain (PSD) and multidomain (MD) ranges calculated for magnetite are indicated, as well as mixing lines between SD and MD and between SD and superparamagnetic (SP) of different sizes are also indicated. Unheated subsamples and subsamples previously heated are denoted by black and red circles, respectively. (For interpretation of the references to color in this figure legend, the reader is referred to the web version of this article.)

We measured hysteresis loops on fresh subsamples (SR1, JG2, and SR3) and samples previously heated to 400 °C in IW conditions and 800 °C in IW-3 conditions (samples 7B3 and SR1a, respectively) with vibrating sample magnetometers at the Institute of Rock Magnetism (maximum applied field 1.5 T) and CEREGE (maximum applied field 1 T) and with a Princeton Measurements Corporation Micromag 2900 alternating gradient force magnetometer (AGFM) in the Rutgers University Paleomagnetism Laboratory. The measured M_{rs}/M_s values and ratios of coercivity (B_c) to coercivity of remanence (B_{cr}) for all subsamples indicate a mean grain PSD grain size with a possible small contribution of superparamagnetic (SP) grains (Dunlop, 2002; Einsle et al., 2016) (Table S3 and Fig. 4). The presence of SP grains and/or multidomain (MD) grains is also indicated by the observation of remanence decay experienced during warming of a low-temperature saturation remanence (Fig. S3B).

We also measured first-order reversal curves (FORC) (Harrison and Feinberg, 2008) for one fresh and two heated subsamples with the Rutgers AGFM. The FORC data were processed using the

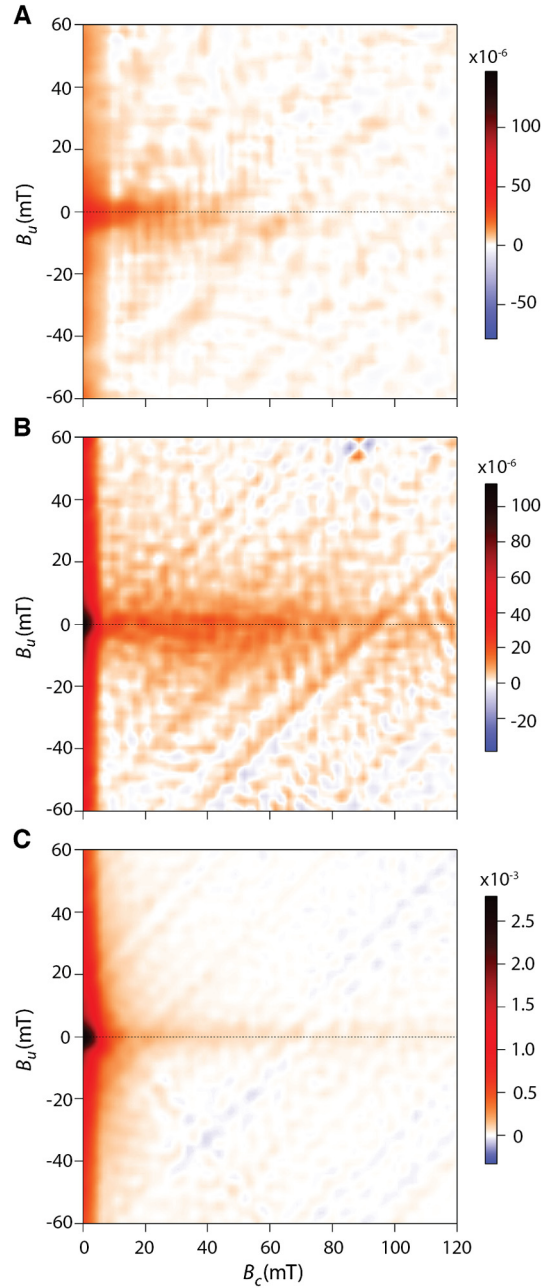


Fig. 5. FORC diagrams for NWA 7325. Shown is B_u (a measure of magnetostatic interactions) on the ordinate versus B_c (coercivity) on the abscissa. The color bar shows the probability density of hysterons belonging to a given combination of B_u and B_c . (A) Fresh subsample SR3. (B) Subsample 7B3C, previously heated to 400 °C in IW conditions. (C) Subsample SR1a, previously heated to 800 °C in IW-3 conditions. (For interpretation of the colors in this figure, the reader is referred to the web version of this article.)

software package FORCinel v. 2.01 (Harrison and Feinberg, 2008) with a smoothing factor of 6 (for fresh subsample SR3) and 3 (for heated subsamples 7B3C and SR1a) (Fig. 5). The magnetization of the fresh subsample SR3 is relatively weak, with a barely distinguishable narrow central ridge with coercivity B_c ranging up to 80 mT, consistent with PSD FeNi grains and a weak low-coercivity ($B_c < 10$ mT) signal with a wide range in H_u , indicative of MD ferromagnetic grains (Fig. 5A). The FORC diagram of heated subsample 7B3C (Fig. 5B) shows a clear narrow high coercivity central ridge, accompanied by an even stronger low coercivity signal, while subsample SR1a (Fig. 5C) shows an even stronger and wider low coercivity signal and virtually no high coercivity central ridge.

The FORC diagrams of the fresh and heated-to-400 °C subsamples indicate a mixture of PSD grains, while the heated-to-800 °C subsample has a larger contribution from MD grains, indicating that the 800 °C heating treatment severely altered the mineralogy of the magnetic grains within NWA 7325 even in the controlled $fO_2 = IW-3$ environment.

These results are consistent with the conclusions in Section 3.1 and 3.2. All told, a diversity of imaging and rock magnetic techniques establishes that NWA 7325 contains dominantly single-phase FeNi martensite grains with sizes of 0.1–1 μm . These grains should be dominantly in the PSD vortex state, which has recently been shown to behave like stable uniaxial single domain particles with high unblocking and blocking temperatures and high resistance to remagnetization by hand magnets and viscous relaxation (Almeida et al., 2016; Einsle et al., 2016). In particular, any remanence in NWA 7325 that formed in the early solar system would likely have been stable against viscous decay over the history of the solar system: Néel theory shows that single domain grains with 1-h blocking temperatures $> \sim 200$ °C would be stable over 4.5 Gy at 0 °C (Garrick-Bethell and Weiss, 2010); a similar conclusion likely holds for the fine PSD grains in NWA 7325 (e.g., Winklhofer et al., 1997). This means that NWA 7325 has unusually high magnetic recording fidelity compared to most FeNi-bearing achondrites (Weiss et al., 2010).

4. Demagnetization of NRM

4.1. Methods

We analyzed the NRM of subsamples from 14 parent stones acquired by S. Ralew with masses ranging from 0.3–2.1 g. All NRM and associated demagnetization measurements were conducted in the MIT Paleomagnetism Laboratory inside a shielded room (DC field < 200 nT) using a 2G Enterprises Superconducting Rock Magnetometer (SRM) 755 equipped with automated AF demagnetization and remagnetization equipment (Kirschvink et al., 2008). Demagnetization data will be posted in the Magnetics Information Consortium (MagIC) database (<https://www2.earthref.org/MagIC/>). Most sample handling was conducted in a class $\sim 10,000$ clean laboratory inside this shielded room. As expected for desert meteorites, most of these stones were found to be essentially completely remagnetized by collectors' hand magnets, as indicated by ratios of NRM to SIRM $> 10\%$. However, we found that at least 4 of these stones escaped being touched with a hand magnet as indicated by a lack of high-intensity NRM overprints. We selected one of these stones, NWA 7325 sample B7 (mass of 1.55 g) for more detailed paleomagnetic analyses.

Sample B7 contained no obvious fusion crust and showed few macroscopic signs of weathering. We measured nine mutually oriented subsamples with masses ranging from 70 to 107 mg cut from parent sample B7 using a wire saw lubricated with alcohol in our shielded clean laboratory. Three of these samples (B71–B73) were subjected to static three axis AF demagnetization up to either 85 or 150 mT. These samples were mounted with cyanoacrylate on to GE 124 silica glass slides with moments $< 10^{-11}$ Am². The sample magnetic moments were measured after AF application in each of the three orthogonal directions. To reduce the acquisition of spurious remanence, we repeated AF applications 2–4 times for each AF level and averaged the measurements following the Zijderveld–Dunlop method (Tikoo et al., 2014). The remaining six subsamples (B74–B79) were thermally demagnetized up to either 400, 515 or 800 °C in a controlled H_2 – CO_2 atmosphere (Suavet et al., 2014) under IW-3 conditions in an ASC Scientific Model TD48-SC thermal demagnetizer [see Section 3.2]. Samples B74 and B75 were heated without any disk mounts or adhesives but measured on GE 124 disks using magnetically clean tape (total moment $< 1 \times 10^{-11}$ Am²), while B76–B79 were glued to

GE 124 disks with potassium silicate for the entire demagnetization and measurement process (total moment $< 1 \times 10^{-11}$ Am²). Two of the thermally-demagnetized samples (B74 and B75) were pre-treated with AF demagnetization to 5 mT prior to beginning thermal demagnetization to remove any weak IRM overprints (although, as described in Section 4.2, such overprints were found not to be present). The three-axis moment noise level of the MIT 2G SRM superconducting sensors under typical operating conditions in the MIT Paleomagnetism Laboratory is $< 1 \times 10^{-12}$ Am² (Wang et al., 2017). As such, in this study, the moments of the silica disk mounts are the main factor limiting the sensitivity of the 2G SRM measurements, such that our estimated moment uncertainty here is $0.5\text{--}1 \times 10^{-11}$ Am².

4.2. NRM components

NRM components were identified using principal component analysis (PCA) (Kirschvink, 1980). AF and thermal demagnetization isolated two NRM components that are approximately unidirectional across the parent sample (Figs. 6 and 7 and Table S4). A relatively strong low coercivity (LT), low temperature (LT) component unblocked up to a peak AF of 4–16 mT and a peak temperature of 165–340 °C. Two subsamples contained a weak, medium coercivity (MC), medium temperature (MT) component that unblocked from the end of the LC/LT component up to a peak AF of 20.5 mT and temperature of 378 °C. After removal of the MC/MT component, further demagnetization produced an approximately spherical cloud of vector endpoints with no demagnetization. The observed moment variations at this point were ~ 50 times the noise limit imposed by the silica holder moments (see Fig. 6 legend) and so indicate near-total demagnetization of the NRM in combination with spurious remanence acquisition from the AF waveform rather than measurement noise (see Section 4.1). PCA fits to this high coercivity (HC) and high temperature (HT) range not constrained to the origin have maximum angular deviation (MAD) values ranging from 30–46°. The high MAD values and lack of decay in magnetization intensity are strong indicators that there is no NRM blocked in the HC/HT range.

5. Paleointensity experiments

5.1. Overview

We conducted paleointensity experiments using both thermal and non-thermal methods. The advantage of thermal methods is that, if alteration can be mitigated, they directly reproduce the acquisition process by which any thermoremanent NRM was acquired and so in principle permit more accurate paleointensities than non-thermal methods. However, the accuracy of thermal methods is fundamentally limited by thermochemical alteration of the samples during heating (i.e., due to oxidation reactions and due to conversion of martensite to taenite). As shown in Section 3.2, our thermal alteration experiments demonstrated that even in our controlled atmosphere, NWA 7325 experiences significant thermochemical alteration above 400 °C.

5.2. Methodology

We estimated the paleointensities for the components in NWA 7325 using two nonthermal (ARM- and IRM-based) multicomponent paleointensity techniques and one TRM-based multicomponent paleointensity technique (see supplementary text). All three techniques (ARM, IRM, and thermal) produced broadly similar paleointensities (Fig. 8). The LC/LT components for 9 subsamples have a mean paleointensity of 23 ± 5 μT , while our mean MC paleointensity estimate for subsample B73 was 7.5 ± 2.1 μT [uncertainties are 1 standard deviation (σ) from the mean]. Nearly all HC/HT paleointensity estimates were within error of zero. The ARM, IRM, and

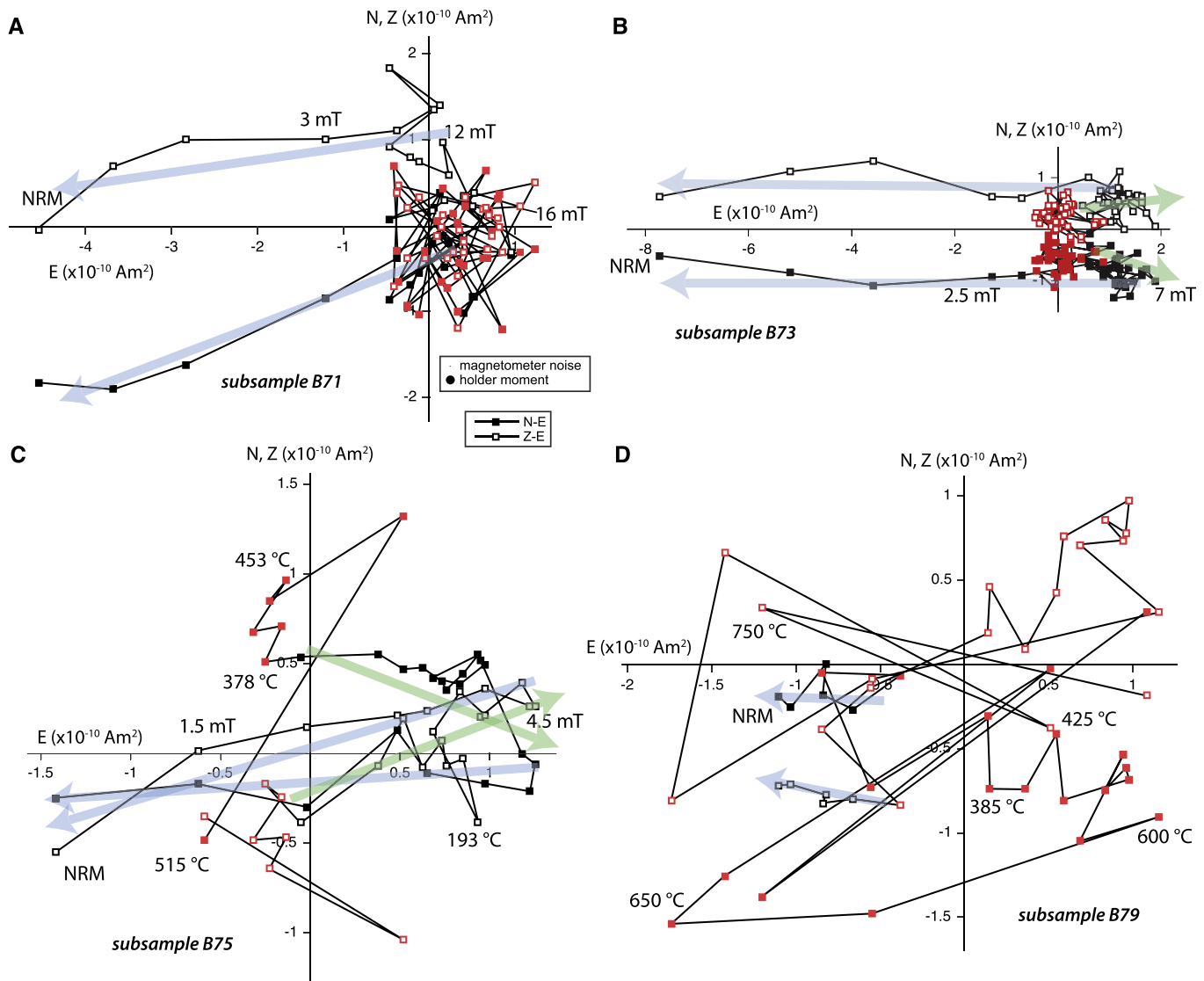


Fig. 6. AF and thermal demagnetization experiments on NRM in NWA 7325. Shown is a two-dimensional projection of the endpoints of the NRM vector during laboratory demagnetization. Solid (open) symbols represent end points of magnetization projected onto the horizontal N–E (vertical Z–E) planes (see left legend). Blue and green arrows denote LC/LT and MC/MT component directions, respectively. Sensor noise of MIT 2G SRM and quartz disk holder moment for measurements in (A) are shown by two tiny black circles in top legend. (A) Subsample B71. (B) Subsample B73. (C) Subsample B75. (D) Subsample B79. Peak fields and temperatures for demagnetization steps are labeled in mT and °C, respectively.

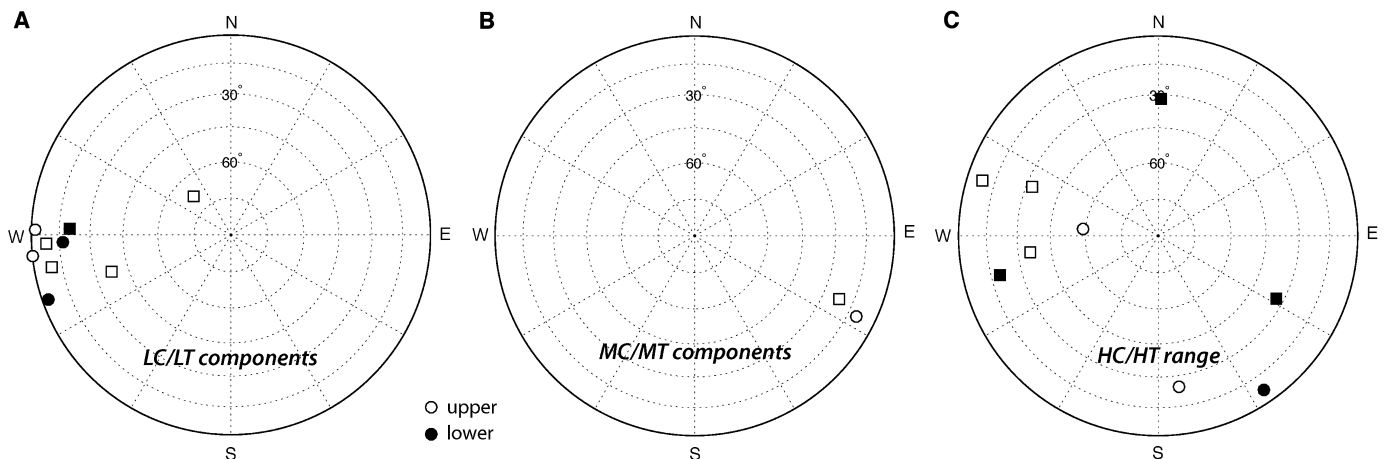


Fig. 7. NRM component directions observed in NWA 7325. Shown are equal area stereographic projections of Fisher mean directions (symbols) and associated maximum angular deviation values (surrounding ellipses) obtained from principal component analyses. (A) LC (circles) and LT (squares) component directions. (B) MC (circles) and MT (squares) component directions. (C) HC (circles) and HT (squares) magnetization directions.

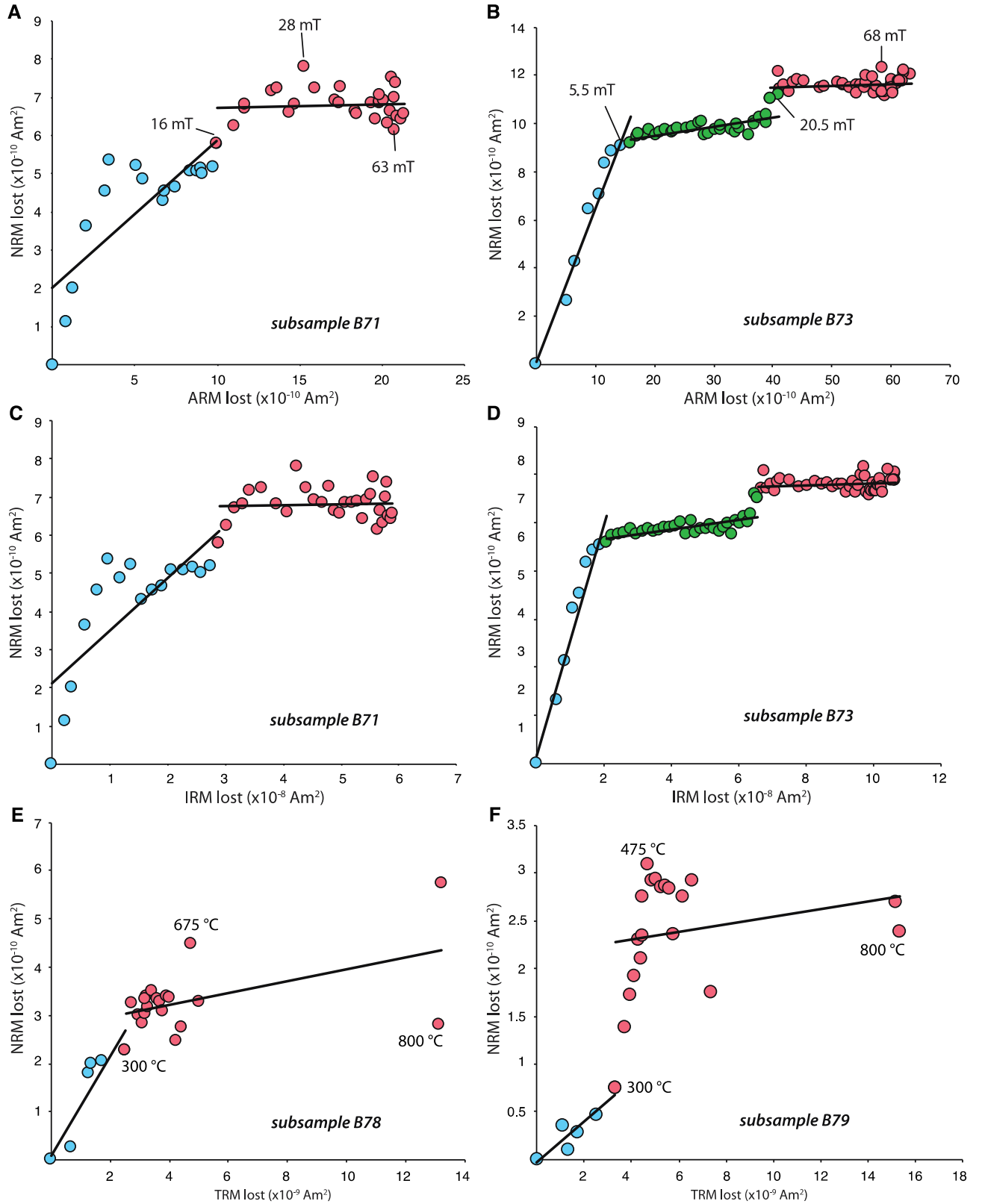


Fig. 8. Paleointensity experiments on NWA 7325. (A, B) NRM lost as a function of ARM (AF of 200 mT, bias field of 0.2 mT) lost during AF demagnetization for subsample B71 (A) and B73 (B). (C, D) NRM lost as a function of near-saturation IRM (200 mT) lost during AF demagnetization for subsamples B71 (C) and B73 (D). (E, F) NRM lost as a function of TRM (800 °C and 30 μT field) lost during thermal demagnetization for subsamples B78 (E) and B79 (F). Points corresponding to the LC/LT and MC/MT components and HC/HT magnetization are colored blue, green and red, respectively. Selected AF and thermal demagnetization steps are labeled. (For interpretation of the references to color in this figure legend, the reader is referred to the web version of this article.)

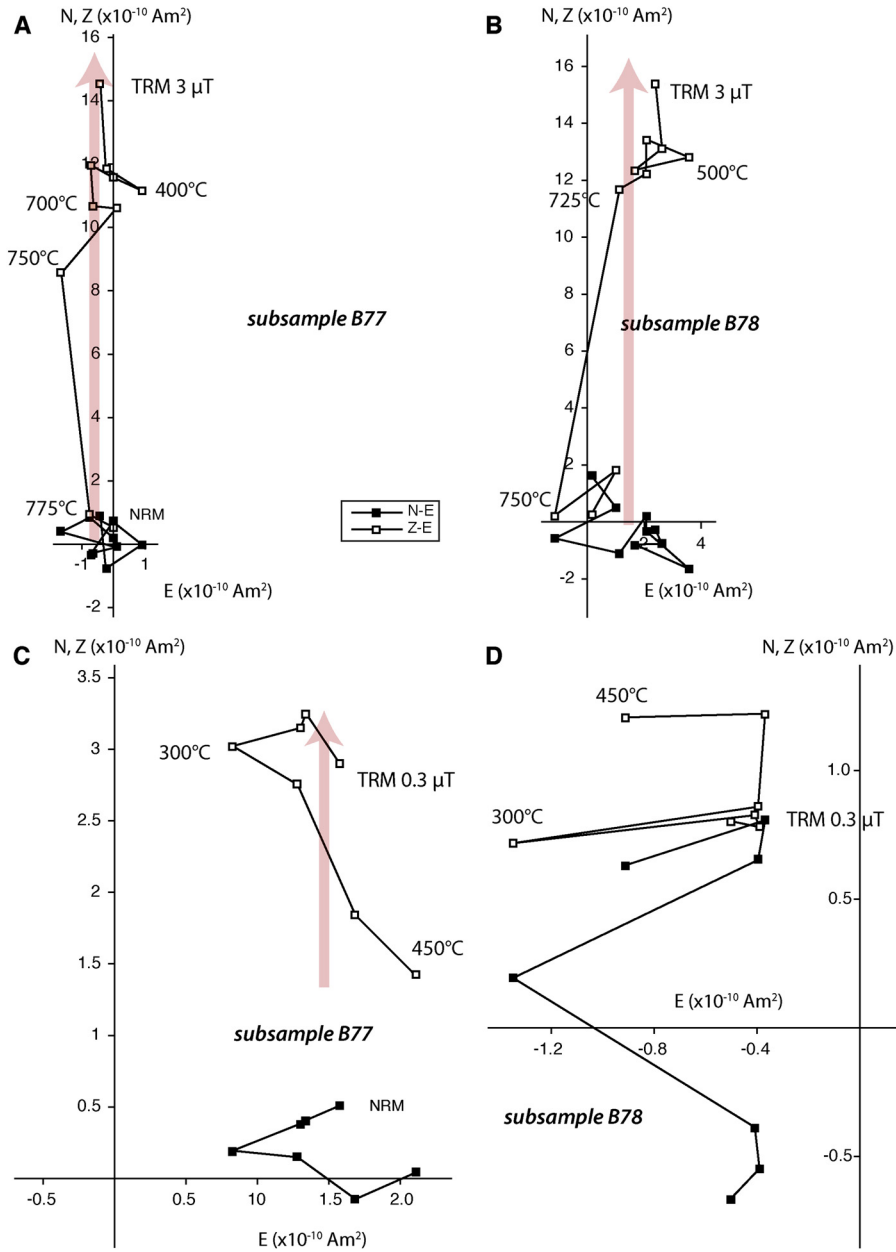


Fig. 9. Thermal paleointensity fidelity test using directional criteria. Shown is the fidelity by which an 800 °C total TRM can be isolated by thermal demagnetization. (A, B) Thermal demagnetization of TRM acquired in a vertical (positive Z) 3 μT field for samples B77 and B78. (C, D) Thermal demagnetization of TRM acquired in a vertical (positive Z) 0.3 μT field for samples B77 and B78. Red arrows show where demagnetization of the TRM is visible. (For interpretation of the references to color in this figure legend, the reader is referred to the web version of this article.)

800 °C total paleointensity experiments provided the most sensitive constraints; their mean HC/HT paleointensity is $1.7 \pm 1.4 \mu\text{T}$ ($\pm 1-\sigma$), indicating essentially zero-field conditions during the time of final cooling. Note that these uncertainties do not take into the account the systematic uncertainties associated with the unknown efficiency of TRM to ARM and IRM. Taking these into consideration (supplementary text), the mean paleointensities values quoted above are estimated to have a 2- σ error of a factor of 5.

5.3. Paleointensity fidelity tests

Our demagnetization of NRM and associated paleointensity experiments suggest that grains in the HC/HT range do not carry NRM, such that the meteorite last cooled from the martensite ordering temperature in a near-zero field. We now seek to place an upper limit on the field environment at the time of last cool-

ing by (a) determining the minimum paleointensity recoverable by the nonthermal techniques used in Section 5.2 and that (b) could produce a TRM component that exhibits linear, stable demagnetization when thermally demagnetized following our techniques used in Section 4.1. The details of our experiments are described in the supplementary materials. Method (a) shows that we can retrieve paleointensity estimates from NWA 7325 down to TRM-equivalent fields as low as $\sim 6 \mu\text{T}$ (Table S6), but as discussed in Section 5.2, this value has a 2- σ uncertainty of a factor of 5. Method (b) shows that TRM produced by laboratory fields as weak as $\sim 0.3 \mu\text{T}$ can just marginally be isolated by our thermal demagnetization methods (Fig. 9). Given that our thermal alteration tests (Section 3.2), suggest that heating to 800 °C increases ARM by a factor of ~ 10 , these data suggest our thermal demagnetization protocol can isolate ancient TRM produced by paleofields of $0.3 \times 10 = 3 \mu\text{T}$. Import-

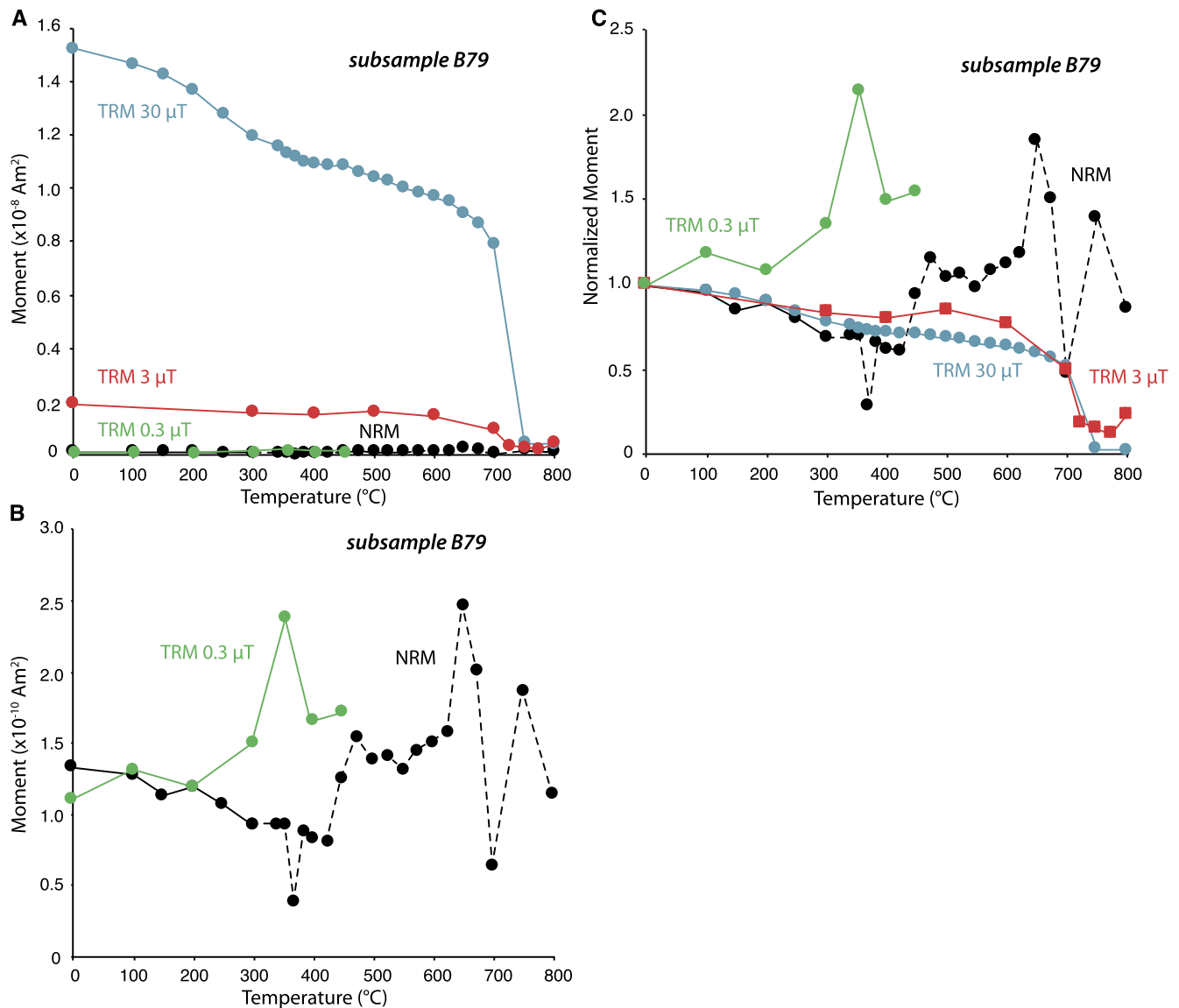


Fig. 10. Thermal demagnetization of NRM (black curve and points) compared to total TRM acquired from cooling in a field of 800 $^{\circ}\text{C}$ in fields of 30, 3, and 0.3 μT (blue, red, and green curves and points, respectively) for sample B79. (A) All data, expressed as moment as a function of temperature. (B) Zoom into NRM and 0.3 μT TRM data from (A). (C) Moment normalized to moment at room temperature before starting thermal demagnetization. NRM loses directional stability by a demagnetization temperature of 300 $^{\circ}\text{C}$; directionally unstable data at higher demagnetization temperatures are connected with a dashed line. (For interpretation of the references to color in this figure legend, the reader is referred to the web version of this article.)

tantly, this 3 μT value is not subject to the high uncertainties associated with calibration of ARM/TRM and IRM/TRM for our non-thermal paleointensities because it was estimated by direct application of a TRM. The nominal ~ 6 μT and 3 μT upper limits from methods (a) and (b) are similar, although slightly less restrictive than, the ~ 1.7 μT upper limit inferred from our paleointensity experiments on the HC/HT magnetization range (Fig. 10).

6. Meaning of magnetization in NWA 7325

The preceding experiments make it clear that NWA 7325 does not contain a total TRM. Its NRM essentially completely demagnetizes by peak laboratory temperatures of just 165–378 $^{\circ}\text{C}$ (below the temperatures at which significant thermochemical alteration occurs) even though it contains ferromagnetic grains that can readily acquire weak-field (< 3 μT) TRM that is stable to thermal demagnetization temperatures of > 750 $^{\circ}\text{C}$. Furthermore its NRM

essentially completely AF demagnetizes by just 4–20.5 mT; such low coercivity grains are readily remagnetized by shocks of just 2 GPa that would otherwise leave virtually no petrographic expression (Weiss et al., 2010) and anyway are below the shock pressures known to have been experienced by the meteorite (Section 2). Most of the NRM that is present in NWA 7325 is in the form of the LC/LT component. Its unidirectionality across the parent sample, ~ 23 μT paleointensity, and low peak unblocking temperature are all consistent with origin as a VRM in the Earth's field following landing on Earth.

The origin of the MC/MT component, unambiguously present in just two of the nine analyzed subsamples is more obscure given its weak paleointensity (about 10% of the Earth's field); it might be another VRM component that has weak (i.e., below that of Earth's field) apparent paleointensities due to changes in the meteorite's position with respect to the Earth's field since landing, or perhaps it is an inefficient crystallization remanent magnetization (CRM) carried by small quantities of secondary ferromagnetic

minerals produced during terrestrial weathering. A CRM is broadly consistent with the $\sim 1.8 \times 10^{-10}$ and $\sim 1.3 \times 10^{-10}$ Am² intensities of the MC/MT components in subsamples B73 and B75 given the $\sim 5.7 \times 10^{-5}$ Am² SIRM for magnetite in NWA 7325 inferred from the low-temperature experiments (Section 3.1): for a typical efficiency of CRM produced in an Earth-strength field to SIRM of 0.2–0.02% (Dunlop and Özdemir, 1997), we estimate CRM carried by magnetite in these subsamples should have an intensity of $\sim 0.6\text{--}6 \times 10^{-10}$ and $1\text{--}10 \times 10^{-10}$ Am², respectively.

In any case, after laboratory demagnetization of the LC/LT and MC/MT components, the remaining HC/HT magnetization in NWA 7325 is highly nonunidirectional across the parent sample and has paleointensities within error of zero. The HC/HT magnetization is likely a combination of spurious remanence acquired during the AF and thermal demagnetization process (e.g., due to imperfections in the AF waveform and/or intragrain interaction fields, respectively) (Tikoo et al., 2014) and possibly also spontaneous remanence. We conclude that the field on the parent body of NWA 7325 when it last cooled from its 780 °C Curie temperature was most likely <1.7 μT. Given that the estimated closure temperature of Mg diffusion in NWA 7325 anorthite exceeds 780 °C, we conclude that these zero-field conditions are best dated by the meteorite's Al–Mg model age of 4563.09 ± 0.26 Ma (supplementary online text).

7. Implications

NWA 7325 is the first recognized small-body achondrite robustly shown to have formed in near-zero field conditions in the early solar system [see original report by Weiss et al. (2013)]. Although numerous basaltic achondrites have been previously been found to have nonunidirectional and highly unstable NRMs, most of these samples have very poor magnetic recording properties likely due to the coarse multidomain grain sizes of their constituent metal grains (Weiss et al., 2010). Furthermore, in nearly all such cases, quantitative limits on the maximum intensity and timing of the field experienced by these samples during final cooling were not established. A recently-discovered exception is the fine-grained angrites, which evidently also cooled in a near-zero paleofield (<0.7 μT at 4563.5 ± 0.1 Ma) (Wang et al., 2017). The weakest robustly-recovered paleointensity recovered from an achondrite is the ~ 12 μT value (with a lower bound of 2 μT given the uncertainties in the non-thermal paleointensity technique; see above) measured for the eucrite ALHA81001 (Fu et al., 2012). Additionally, two main group pallasites were recently shown to have formed within a minimum field strength of $\sim 1\text{--}7$ μT; this was interpreted as a record of fields from crustal remanence that itself was the product of an earlier thermal convection core dynamo (Nichols et al., 2016).

Although our <1.7 μT paleointensity constraint from NWA 7325 provides no robust record of magnetic fields on the parent body, it is not sufficiently sensitive to exclude the existence of a weak dynamo or crustal remanent fields at the time of final cooling. In particular, dynamo scaling laws indicate the feasibility of surface fields from planetesimal dynamos weaker than 3 μT (Formisano et al., 2016; Weiss et al., 2010). Furthermore, the crustal fields expected for a body whose crust had been magnetized by even a strong dynamo surface field can also easily be weaker than 3 μT. Following Fu et al. (2012), the maximum possible crustal field at a demagnetized location within the crust of a body carrying a TRM produced by an ancient dynamo field of 100 μT is given by

$$B_{\text{crust}} < \mu_0 M_{\text{TRM}} \rho$$

where $M_{\text{TRM}} \sim 0.03 M_{\text{rs}}$ for a TRM in a paleofield of 100 μT, μ_0 is the permeability of free space, and ρ is the crustal density. Assuming the crust is made out of NWA 7325-like material (for which

$\rho \sim 3000$ kg m⁻³ and $M_{\text{rs}} = 10^{-3}$ Am² kg⁻¹; see Table S3), we estimate $B_{\text{crust}} < 0.1$ μT. Therefore, it is entirely possible that the parent body of NWA 7325 generated a strong (>100 μT) dynamo magnetic field prior to the meteorite's period of final cooling time, a weaker dynamo (<1.7 μT) during this cooling period, or an arbitrarily strong field after this period.

Our nominal <1.7 μT constraint is also consistent with Mercury's $\sim 0.1\text{--}0.7$ μT present day surface field (Stevenson, 2010). However, this coincidence may have limited significance for the hypothesis that NWA 7325 originates from Mercury given that the age of its magnetization is ~ 4500 Ma, not the present. Furthermore, NWA 7325's 4563 Ma formation age would make it far older than the oldest large-scale surfaces dated by crater counting (4000–4100 Ma) on Mercury (Koefoed et al., 2016). Therefore, although our magnetic data are formally consistent with formation of NWA 7325 in Mercury's present-day field, we consider a Mercury origin for NWA 7325 unlikely.

Our measurements on NWA 7325 require that all magnetic field sources at the meteorite's location were below ~ 1.7 μT at 4563.09 ± 0.26 Ma. This includes core dynamo, nebular, and impact-generated fields, which have been predicted under some conditions to well exceed our nominal 1.7 μT constraint. A near-zero nebular field at this time in turn supports the recent conclusion that the solar nebula had likely dissipated by 4 million years after CAIs (Wang et al., 2017). Our field constraint also applies to that of the solar wind, which has been proposed to be the source of the strong middle temperature (MT) component observed in CV chondrites (Tarduno et al., 2016). In fact, our results show that the intensity of the solar wind field was also below the ~ 60 and ~ 3 μT paleointensities measured from the CV chondrites Allende and Kaba, respectively (Carpözen et al., 2011; Gattacceca et al., 2016). On the other hand, the latter high paleointensities are consistent with a core dynamo origin for this magnetization. Finally, our analysis of NWA 7325 demonstrates that we can successfully and sensitively identify near-zero field constraints from meteorites. This gives greater confidence to the many other meteorite studies that have inferred the existence of past magnetic fields.

8. Summary

- NWA 7325 is an ungrouped achondrite from a differentiated planetesimal.
- The meteorite last cooled from above the 780 °C in essentially zero-field conditions (nominally <1.7 μT, or possibly with an upper limit as high as <9 μT considering uncertainties in non-thermal paleointensity calibration coefficients).
- This requires that any dynamo field as well as any externally generated fields like those from the nebula and solar wind were <1.7 μT at an estimated age 4563.09 ± 0.26 Ma.
- NWA 7325 is the first small body achondrite recognized to be unmagnetized despite having originated from a body that likely formed a metallic core.
- Our paleointensity constraint on NWA 7325 is consistent with the field strength of present-day Mercury, but the meteorite's great age makes a Mercury origin unlikely.
- Our ability to recognize unmagnetized achondrites provides a control that builds confidence in the widespread identification of magnetized achondrites from other bodies.

Acknowledgements

We thank S. Ralew for proving samples of NWA 7325 for study and Neel Chatterjee for assistance with electron microscopy measurements. We gratefully acknowledge the use of the LeRoy Eyring Center for Solid State Science at Arizona State University. BPW

thanks the NASA Emerging Worlds program grant #NNX15AH72G, the NASA Solar System Exploration and Research Virtual Institute grant #NNA14AB01A, the U.S. Rosetta program (JPL award #NM0710889), and a generous gift from Thomas F. Peterson, Jr. BD thanks the Massachusetts Institute of Technology Undergraduate Research Opportunities Program for support. JG acknowledges funding from the ANER (grant ANR-14-CE33-0012) and the Marie Curie People Programme (FP7/2007–2013, REA grant 29835). We also thank the Rutgers Paleomagnetism Laboratory and the Institute of Rock Magnetism for enabling some of our rock magnetic measurements. Measurements at NSLS, BNL were supported by the U.S. DOE under contract #DE-AC02-98CH10886.

Appendix A. Supplementary material

Supplementary material related to this article can be found online at <http://dx.doi.org/10.1016/j.epsl.2017.03.026>.

References

- Almeida, T.P., Muxworthy, A.R., Kovács, A., Williams, W., Brown, P.D., Dunin-Borkowski, R.E., 2016. Direct visualization of the thermomagnetic behavior of pseudo-single-domain magnetite particles. *Sci. Adv.* 2, e1501801.
- Archer, G.J., Walker, R.J., Irving, A.J., 2015. Highly siderophile element and ^{187}Re – ^{187}Os isotopic systematics of ungrouped achondrite Northwest Africa 7325. *Lunar Planet. Sci. Conf. Abstr.* XLVI, 1987.
- Baker, D.R., Mancini, L., Polacci, M., Higgins, M.D., Gualda, G.A.R., Hill, R.J., Rivers, M.L., 2012. An introduction to the application of X-ray microtomography to the three-dimensional study of igneous rocks. *Lithos* 148, 262–276.
- Barrat, J.A., Greenwood, R.C., Verchovsky, A.B., Gillet, P., Bollinger, C., Langlade, J.A., Liorzou, C., Franchi, I.A., 2015. Crustal differentiation in the early solar system: clues from the unique achondrite Northwest Africa 7325 (NWA 7325). *Geochim. Cosmochim. Acta* 168, 280–292.
- Berndt, T., Muxworthy, A.R., Fabian, K., 2016. Does size matter? Statistical limits of paleomagnetic field reconstruction from small rock specimens. *J. Geophys. Res.* 121. <http://dx.doi.org/10.1002/2015JB012441>.
- Bryson, J.F.J., Nichols, C.I.O., Herrero-Albillos, J., Kronast, F., Kasama, T., Alimadadi, H., van der Laan, G., Nimmo, F., Harrison, R.J., 2015. Long-lived magnetism from solidification-driven convection on the pallasite parent body. *Nature* 517, 472–475.
- Carporzen, L., Weiss, B.P., Elkins-Tanton, L.T., Shuster, D.L., Ebel, D.S., Gattacceca, J., 2011. Magnetic evidence for a partially differentiated carbonaceous chondrite parent body. *Proc. Natl. Acad. Sci. USA* 108, 6386–6389.
- Cerantola, V., Walte, N.P., Rubie, D.C., 2015. Deformation of a crystalline olivine aggregate containing two immiscible liquids: implications for early core–mantle differentiation. *Earth Planet. Sci. Lett.* 417, 67–77.
- Cisowski, S.M., 1991. Remanent magnetic properties of unbrecciated eucrites. *Earth Planet. Sci. Lett.* 107, 173–181.
- Cournède, C., Gattacceca, J., Gounelle, M., Rochette, P., Weiss, B.P., Zanda, B., 2015. An early solar system magnetic field recorded in CM chondrites. *Earth Planet. Sci. Lett.* 410, 62–74.
- Dunlop, D.J., 2002. Theory and application of the Day plot (M_{rs}/M_s versus H_{cr}/H_c) 1. Theoretical curves and tests using titanomagnetite data. *J. Geophys. Res.* 107. <http://dx.doi.org/10.1029/2001JB000486>.
- Dunlop, D.J., Özdemir, O., 1997. *Rock Magnetism: Fundamentals and Frontiers*. Cambridge University Press, New York.
- Einsle, J.F., Harrison, R.J., Kasama, T., Conbhui, P.O., Fabian, K., Williams, W., Woodland, L., Fu, R.R., Weiss, B.P., Midgley, P.A., 2016. Multi-scale three-dimensional characterisation of iron particles in dusty olivine: implications for paleomagnetism of chondritic meteorites. *Am. Mineral.* 101, 2070–2084.
- Elkins-Tanton, L.T., Weiss, B.P., Zuber, M.T., 2011. Chondrites as samples of differentiated planetesimals. *Earth Planet. Sci. Lett.* 305, 1–10.
- Fischer, S.R., Fu, R.R., Weiss, B.P., Li, L., Gattacceca, J., Sonzogni, C., 2013. Paleomagnetic detection of magnetic fields on a differentiated asteroid during the dynamo epoch. In: Fall AGU Meeting, GP41D-1166.
- Formisano, M., Federico, C., De Angelis, S., De Sanctis, M.C., Magni, G., 2016. A core dynamo in Vesta? *Mon. Not. R. Astron. Soc.* 458, 695–707.
- Fu, R.R., Weiss, B.P., Shuster, D.L., Gattacceca, J., Grove, T.L., Suavet, C., Lima, E.A., Li, L., Kuan, A.T., 2012. An ancient core dynamo in asteroid Vesta. *Science* 338, 238–241.
- Garrick-Bethell, I., Weiss, B.P., 2010. Kamacite blocking temperatures and applications to lunar magnetism. *Earth Planet. Sci. Lett.* 294, 1–7.
- Gattacceca, J., Weiss, B.P., Gounelle, M., 2016. New constraints on the magnetic history of the CV parent body and the solar nebula from the Kaba meteorite. *Earth Planet. Sci. Lett.* 455, 166–175.
- Gilmour, J.D., Crowther, S.A., 2017. The I-Xe chronometer and its constraints on the accretion and evolution of planetesimals. *Geochim. J.* 51, 69–80.
- Harrison, R.J., Feinberg, J.M., 2008. FORCinel: an improved algorithm for calculating first-order reversal curve distributions using locally weighted regression smoothing. *Geochim. Geophys. Geosyst.* 9, Q05016.
- Irving, A.J., Kuehner, S.M., Bunch, T.E., Ziegler, K., Chen, G., Herd, C.D.K., Conrey, R.M., Ralew, S., 2013. Ungrouped mafic achondrite Northwest Africa 7325: a reduced, iron-poor cumulate olivine gabbro from a differentiated planetary parent body. *Lunar Planet. Sci. Conf. Abstr.* XLIV, 2164.
- Kirschvink, J.L., 1980. The least-squares line and plane and the analysis of paleomagnetic data: examples from Siberia and Morocco. *Geophys. J. R. Astron. Soc.* 62, 699–718.
- Kirschvink, J.L., Kopp, R.E., Raub, T.D., 2008. Rapid, precise, and high-sensitivity acquisition of paleomagnetic and rock-magnetic data: development of a low-noise automatic sample changing system for superconducting rock magnetometers. *Geochim. Geophys. Geosyst.* 9, Q05Y01. <http://dx.doi.org/10.1029/2007GC001856>.
- Koefoed, P., Amelin, Y., Yin, Q.-Z., Wimpenny, J., Sanborn, M.E., Izuka, T., Irving, A.J., 2016. U–Pb and Al–Mg systematics of the ungrouped achondrite Northwest Africa 7325. *Geochim. Cosmochim. Acta* 183, 31–45.
- Krauss, G., 2005. *Steels: Processing, Structure, and Performance*. ASM International, Materials Park, OH.
- Kruijer, T.S., Touboul, M., Fischer-Gödde, M., Bermingham, K.R., Walker, R.J., Klein, T., 2014. Protracted core formation and rapid accretion of protoplanets. *Science* 344, 1150–1154.
- Lima, E.A., Weiss, B.P., 2016. Ultra-high sensitivity moment magnetometry of geological samples using magnetic microscopy. *Geochim. Geophys. Geosyst.* 17. <http://dx.doi.org/10.1002/2016GC006487>.
- Moskowitz, B.M., 1981. Methods for estimating Curie temperatures of titanomagnetites from experimental $J_s - T$ data. *Earth Planet. Sci. Lett.* 53, 84–88.
- Nichols, C.I.O., Bryson, J.F.J., Herrero-Albillos, J., Kronast, F., Nimmo, F., Harrison, R.J., 2016. Pallasite paleomagnetism: quiescence of a core dynamo. *Earth Planet. Sci. Lett.* 441, 103–112.
- Nimmo, F., 2009. Energetics of asteroid dynamos and the role of compositional convection. *Geophys. Res. Lett.* 36. <http://dx.doi.org/10.1029/2009GL037997>.
- Özdemir, Ö., Dunlop, D.J., Moskowitz, B.M., 2002. Changes in remanence, coercivity and domain state at low temperature in magnetite. *Earth Planet. Sci. Lett.* 194, 343–358.
- Rückriemen, T., Breuer, D., Spohn, T., 2015. The Fe snow regime in Ganymede's core: a deep-seated dynamo below a stable snow zone. *J. Geophys. Res.* 120, 1095–1118.
- Ruzicka, A., 2014. Silicate-bearing iron meteorites and their implications for the evolution of asteroidal parent bodies. *Chem. Erde* 74, 3–48.
- Scheinberg, A., Elkins-Tanton, L.T., Schubert, G., Bercowski, D., 2015a. Core solidification and dynamo evolution in a mantle-stripped planetesimal. *J. Geophys. Res.* 121. <http://dx.doi.org/10.1002/2015JE004843>.
- Scheinberg, A., Fu, R.R., Elkins-Tanton, L.T., Weiss, B.P., 2015b. Asteroid differentiation: melting and large-scale structure. In: Michel, P., DeMeo, F., Bottke, W.F. (Eds.), *Asteroids IV*. University of Arizona Press, Tucson, pp. 533–552.
- Sternerborg, M.G., Crowley, J.W., 2013. Thermal evolution of early solar system planetesimals and the possibility of sustained dynamos. *Phys. Earth Planet. Inter.* 214, 53–73.
- Stevenson, D.J., 1983. Planetary magnetic fields. *Rep. Prog. Phys.* 46, 555–620.
- Stevenson, D.J., 2010. Planetary magnetic fields: achievements and prospects. *Space Sci. Rev.* 152, 651–664.
- Suavet, C., Weiss, B.P., Grove, T.L., 2014. Controlled-atmosphere thermal demagnetization and paleointensity analyses of extraterrestrial rocks. *Geochim. Geophys. Geosyst.* 15. <http://dx.doi.org/10.1002/2013GC005215>.
- Sutton, S.R., Wirick, S., Goodrich, C.A., 2014. Ungrouped achondrite NWA 7325: titanium, vanadium, and chromium XANES of mafic silicates record highly-reduced origin. *Lunar Planet. Sci. Conf. Abstr.* XLV, 1275.
- Swartzendruber, L.J., Itkin, V.P., Alcock, C.B., 1991. The Fe–Ni (iron–nickel) system. *J. Phase Equilib.* 12, 288–312.
- Tarduno, J.A., Cottrell, R.D., Nimmo, F., Hopkins, J., Voronov, J., Erickson, A., Blackman, E., Scott, E.R.D., McKinley, R., 2012. Evidence for a dynamo in the main group pallasite parent body. *Science* 338, 939–942.
- Tarduno, J.A., O'Brien, T.M., Smirnov, A.V., 2016. Does the magnetization of CV meteorites record a parent body core dynamo? *Lunar Planet. Sci. Conf. Abstr.* XLVII, 2609.
- Tikoo, S.M., Weiss, B.P., Cassata, W.S., Shuster, D.L., Gattacceca, J., Lima, E.A., Suavet, C., Nimmo, F., Fuller, M., 2014. Decline of the lunar core dynamo. *Earth Planet. Sci. Lett.* 404, 89–97.
- Wang, H., Weiss, B.P., Bai, X.-N., Downey, B.G., Wang, J., Wang, J., Suavet, C., Fu, R.R., Zucolotto, M.E., 2017. Lifetime of the solar nebula constrained by meteorite paleomagnetism. *Science* 355, 623–627.
- Wang, J., Chen, Y.-C.K., Yuan, Q., Tkachuk, A., Erdonmez, C., Hornberger, B., Feser, M., 2012. Automated markerless full field hard x-ray microscopic tomography at sub-50 nm 3-dimension spatial resolution. *Appl. Phys. Lett.* 100, 143107.
- Weber, I., Morlok, A., Bischoff, A., Hiesinger, H., Ward, D., Joy, K.H., Crowther, S.A., Jasterzebski, N.D., Gilmour, J.D., Clay, P.L., Wogelius, R.A., Greenwood, R.C., Franchi, I.A., Münker, C., 2016. Cosmochemical and spectroscopic properties of Northwest Africa 7325—a consortium study. *Meteorit. Planet. Sci.* 51, 3–30.

- Weisberg, M.K., McCoy, T.J., Krot, A.N., 2006. Systematics and evaluation of meteorite classification. In: Lauretta, D.S., McSween, H.Y. (Eds.), *Meteorites and the Early Solar System II*. University of Arizona, Tucson, pp. 19–52.
- Weiss, B.P., Gattacceca, J., Stanley, S., Rochette, P., Christensen, U.R., 2010. Paleomagnetic records of meteorites and early planetesimal differentiation. *Space Sci. Rev.* 152, 341–390.
- Weiss, B.P., Gattacceca, J., Suavet, C., Irving, A.J., 2013. Magnetic and nonmagnetic differentiated planetesimals. In: *Workshop on Planetesimal Formation and Differentiation*, Abstract #8047.
- Wilson, L., Keil, K., 2012. Volcanic activity on differentiated asteroids: a review and analysis. *Chem. Erde* 72, 289–321.
- Winklhofer, M., Fabian, K., Heider, F., 1997. Magnetic blocking temperatures of magnetite calculated with a three-dimensional micromagnetic model. *J. Geophys. Res.* 102, 22695–22709.

Supplementary Material for

B. P. Weiss et al. (2016) A Nonmagnetic Differentiated Early Planetary Body *Earth and Planetary Science Letters*

Supplementary Text

1. Age of the magnetic field constraint from NWA 7325

The timing of the paleointensity constraint from NWA 7325 can be constrained using thermochronometers with closure temperatures bracketing the temperatures required to remagnetize martensite in NWA 7325, which range from the peak austenite-finish temperature of 780°C down to below room temperature (see main text). The two chronometers that have been applied to NWA 7325 that should have closure temperatures in this range are the $^{40}\text{Ar}/^{39}\text{Ar}$ and Al-Mg systems. Here we discuss the implications of our $^{40}\text{Ar}/^{39}\text{Ar}$ analyses and those of Weber et al. (2016) on NWA 7325 (Section 1.1) and of existing Al-Mg data for the age of NWA 7325's magnetization constraint (Section 1.2)

1.1. Our $^{40}\text{Ar}/^{39}\text{Ar}$ analyses. We conducted $^{40}\text{Ar}/^{39}\text{Ar}$ stepwise degassing analysis of a neutron-irradiated bulk chip from the meteorite (Fig. S1). For this analysis, we heated the sample using a controlled laser diode and conducted noble gas isotopic analysis at each heating step in the Berkeley Geochronology Center following the procedures of Shuster and Cassata (2015). The observed apparent ages of heating steps ranged from ~200 to >2000 million years ago (Ma). We did not observe statistical concordance between individual step ages, likely due to simultaneous release of Ar from multiple phases in the sample containing variable K concentrations and which experienced variable ^{40}Ar retention since the sample crystallized. We find the best agreement to be between the initial 7 steps, which amount to ~50% of the released gas. The error-weighted mean of these steps is formally 444 ± 7 Ma (Fig. S1 and Table S1), which might be interpreted as a rough upper bound on the timing of the most recent episode of detectable diffusive loss of ^{40}Ar . However, due to the lack of statistical concordance of the results and their disagreement with the data of Weber et al. (2016) (see below), the physical meaning of this age is in doubt. Therefore, we do not use these data to constrain the thermal and magnetic history of NWA 7325.

We favor the $^{40}\text{Ar}/^{39}\text{Ar}$ experiments of Weber et al. (2016) over our experiments for three reasons. First, Weber et al. (2016) measured multiple aliquots (both bulk rock and plagioclase separates) and these yielded similar results. By comparison, we measured a single bulk rock aliquot. Second, Weber et al. (2016)'s experiments yielded well-defined age plateaus, unlike our data. Finally, their ages cluster around the known formation age of NWA 7034 as inferred from U-Pb chronometry.

It is unclear why our results differ so substantially from those of Weber et al. (2016), but one possible clue comes from the fact that the Ar-bearing phase in their bulk rock sample has a Ca/K ratio ranging from $\sim 10^3$ to 10^4 , whereas for our sample the Ca/K ratio of the phase degassing at low fractional ^{39}Ar release was 10 and only briefly rose to 10^4 briefly near the end of our experiment. This suggests the major phase(s) releasing Ar in our experiment were much more K-rich than those in the experiment of Weber et al. (2016). Given that NWA 7325 contains minor weathering minerals (see above) and that the terrestrial ages of NWA meteorites are usually <50 ky (Jull, 2006), one possible explanation for the much younger mean age of our

sample is that it happened to contain more of a secondary K-rich phase produced during residence in the desert, such that our 431 Ma mean age reflects the simultaneous release of Ar from this recent secondary phase and with from ancient (4.5 Ga) plagioclase.

Although we adopt the results of Weber et al. (2016) in this paper, we nevertheless recognize that our inability to reproduce their results means that there is some uncertainty in the $^{40}\text{Ar}/^{39}\text{Ar}$ age of the meteorite.

1.2. Al-Mg ages. Koefoed et al. (2016) found that Al-Mg isotopic analyses of NWA 7325 plagioclase, pyroxene, olivine, and whole rock aliquots defined an isochron with an age of 4563.09 ± 0.26 Ma when anchored to the Pb-Pb age of the angrite D'Orbigny. Although there have been no measurements of the cooling rate of NWA 7325 following the last thermal event that exceeded 780°C , the presence of martensite and lack of tetrataenite indicate a minimum cooling rate for this event of at least several thousand $^\circ\text{C}$ per million years (My^{-1}) (Gattacceca et al., 2014). Assuming a cooling rate of $1000^\circ\text{C My}^{-1}$, measurements by Van Orman et al. (2014) and indicate a closure temperature for the Al-Mg system of $<\sim 600^\circ\text{C}$ for NWA 7325's anorthite composition (An_{85-93}) and for the smallest grain observed grain size (i.e., the population of <20 μm remelted plagioclase laths in the meteorite) (see main text Section 2). For the population of ~ 1 mm sized plagioclase with the same An_{85-93} composition, the measurements of Ito and Ganguly (2005, 2009) and LaTourrette and Wasserburg (1998) indicate a closure temperature of $\sim 800^\circ\text{C}$. Therefore, the closure temperature of the Al-Mg system brackets the remagnetization temperatures of the most stable ferromagnetic grains in NWA 7325. Given the much higher precision of the Al-Mg age relative to that of the $^{40}\text{Ar}/^{39}\text{Ar}$ age of Weber et al. (2016) and given the poor quality of our $^{40}\text{Ar}/^{39}\text{Ar}$ data in particular (see Section 1.1), we adopt the Al-Mg age of 4563.09 ± 0.26 Ma as our best estimate for the age of the magnetization constraint from NWA 7325. The $^{40}\text{Ar}/^{39}\text{Ar}$ plagioclase age of 4481 ± 150 Ma of Weber et al. (2016), which records closure temperatures at temperatures several hundred $^\circ\text{C}$ below that of the Al-Mg system, provides a minimum age for the paleointensity constraint.

2. Paleointensity methods

We used two nonthermal (ARM- and IRM-based) multicomponent paleointensity techniques and one TRM-based multicomponent paleointensity technique.

2.1. ARM and IRM techniques. Our nonthermal methods proceeded as follows. Following, Tikoo et al. (2014) and Gattacceca and Rochette (2004), we computed the vector-subtracted decay of the NRM (ΔNRM) during AF demagnetization versus ARM acquisition (ΔARM) and versus the AF demagnetization of saturation IRM (SIRM) (ΔSIRM). The ARM and IRM paleointensity estimates are given by

$$P_{\text{ARM}} = (\Delta\text{NRM}/\Delta\text{ARM}) \times (b/f') \text{ and} \\ P_{\text{IRM}} = (\Delta\text{NRM}/\Delta\text{IRM}) \times a,$$

respectively, for bias field b (set to either 0.2 or 0.4 mT depending on the subsample) and empirically-determined coefficients f' and a . For a given component, ΔNRM , ΔARM , and ΔIRM are taken over the component's AF range as identified by PCA. As in Tikoo et al. (2012),

we report uncertainties on each paleointensity by calculating the 95% confidence interval on the $\Delta\text{NRM}/\Delta\text{ARM}$ and $\Delta\text{NRM}/\Delta\text{SIRM}$ slope using Student's two-tailed t -test (Weisberg, 1985). These uncertainties do not take into account the uncertain values of f and a . Following earlier studies of metal-bearing samples (Weiss and Tikoo, 2014), we use $f' = 1.34$ and $a = 3000$, which quantify the ratio of TRM to IRM and ARM. These have been observed to vary among natural metal-bearing samples, with a 2-standard deviation ($2\text{-}\sigma$) of a factor of ~ 5 .

2.2. TRM techniques. Our thermal paleointensity experiments were conducted on 6 subsamples using three slightly different methods (Table S5). Subsamples B74 and B75, whose NRMs had been thermally demagnetized to a maximum temperature of 515°C, were each given a 515°C partial TRM (pTRM) in a 50 μT field which was then demagnetized in the same way as the NRM (AF demagnetization to 5 mT followed by thermal demagnetization to 515°C). This low peak temperature (well below the 680°C minimum austenite-finish temperature) was chosen to mitigate thermochemical alteration, but means that much of the high unblocking temperatures in the rock were not accessed (which limits the accuracy of paleointensity constraints on the HT component). Subsamples B76 and B77, whose NRMs had been thermally demagnetized to a maximum temperature of 400°C, were each given a 400°C partial TRM (pTRM) in a 30 μT field which was again demagnetized following the same demagnetization protocol for the NRM (thermal demagnetization to 400°C). After reaching 400°C, these two samples were further demagnetized up to 800°C, which enabled us to characterize NRM demagnetization at unblocking temperatures above those used for the original NRM demagnetization sequence. Subsamples B77 and B78 were analyzed in the same way as B76 and B77 except that instead of a pTRM, they were given a total TRM by heating to 800°C. Thermal paleointensities were calculated using

$$P_{\text{TRM}} = (\Delta\text{NRM}/\Delta\text{TRM}) \times B_{\text{lab}}$$

where B_{lab} is the laboratory field, and ΔNRM and ΔTRM are the vector-subtracted amount of NRM and pTRM or TRM lost over the range of a given component. Uncertainties are calculated as the 95% confidence interval on the $\Delta\text{NRM}/\Delta\text{TRM}$ slope using Student's two-tailed t -test (Weisberg, 1985), while mean uncertainties are weighted by the inverse of the square of the uncertainty (Taylor, 1997). This does not capture the biggest source of uncertainty, which for the case of TRM paleointensity experiments is thermochemical alteration. In particular, our thermal alteration tests (main text Section 3.2) indicate that raw paleointensity values for the three thermal methods computed should be multiplied by factors of ~ 6 , ~ 3 , and ~ 10 , respectively, to take account the increase of TRM efficiency after heating to 515, 400, and 800°C, respectively.

3. Paleointensity fidelity tests

3.1. ARM method. Spurious remanence acquired during the AF demagnetization process limits our ability to retrieve accurate paleointensity estimates for weak paleofields using nonthermal (i.e., AF-based) methods. Following Tikoo et al. (2012), we estimated the minimum paleointensity that our ARM paleointensity method could accurately measure by giving subsamples B71 and B73 each a laboratory ARM (an artificial analog of thermoremanent NRM) which was then three-axis AF demagnetized over the range beginning with the lowermost step of the HT range for each subsample (Table S4) and ending at 85 mT. The laboratory ARMs were

produced using an AF field of 200 mT and bias fields ranging from 4 to 200 μT [corresponding to TRM-equivalent fields from 3 to 150 μT , using $f^* = 1.34$ as discussed above]. The ARM method was then used to retrieve a paleointensity value from each of these laboratory-induced magnetizations for the equivalent AF range of the HC magnetization. We quantified the agreement between the paleointensity estimates and the true TRM-equivalent fields used to produce the artificial NRM using the previously defined difference (D) and error (E) metrics:

$$D = \frac{|L-I|}{L} \cdot 100\%$$

$$E = \frac{W}{L} \cdot 100\%$$

where L is the applied laboratory field, I is the measured paleointensity, and W is the 95% confidence interval on the $\Delta\text{NRM}/\Delta\text{TRM}$ slope using Student's two-tailed t -test (Tikoo et al., 2012; Weisberg, 1985). As previously discussed, we consider the paleointensity to be poorly recovered for laboratory field intensities for which either D or E exceed 100%. The results (Table S6) show that the ARM method can retrieve paleointensity estimates from NWA 7325 down to TRM-equivalent fields as low as ~ 5 -7.5 μT (Table S6). Note that this estimate is a conservative upper limit because spurious remanence was introduced into the sample as part of the ARM acquisition process that produced the artificial NRMs subjected to these tests. On the other hand, this upper limit is subject to the same factor of ~ 5 uncertainty as our ARM paleointensity estimates due to uncertain values of f^* .

3.2. Directional stability during thermal demagnetization. We also tested our ability to isolate magnetization in NWA 7325 produced by weak fields by monitoring the directional stability of laboratory TRM during thermal demagnetization. Following thermal demagnetization of their NRMs, subsamples B76, B77, B78, and B79 were given total TRMs by heating to 800°C and cooling in a field of 0.3 μT ; these TRMs were then thermally demagnetized to 450°C. The samples were then heated to 800°C and cooled in a 3 μT and thermally demagnetized to 800°C. For the 3 μT experiments, all samples exhibited a component oriented in the laboratory field direction that was stable up to at least 750°C (Fig. 9A, B), which is 450°C higher than the peak unblocking temperature of the NRM (Fig. 10). By comparison, for the 0.3 μT experiments, three samples showed no clear component while the fourth showed a weak component approximately oriented in the laboratory field direction and stable to at least 450°C (Fig. 9C, D). The TRM intensity acquired from cooling in a 0.3 μT field is comparable to that of the NRM (Fig. 10).

The 0.3 μT experiments were significantly disadvantaged by the fact that thermal demagnetization was conducted only up to a maximum temperature of 450°C, which is below the temperature at which the majority of thermal unblocking occurs (e.g., Fig. 9A, B). On the other hand, this disadvantage was offset by the fact that our thermal alteration tests (main text Section 3.2) found that heating to 800°C increases ARM by a factor of ~ 10 (Fig. S4). Taking both caveats into consideration, we conclude that our AF and thermal demagnetization methods can accurately retrieve paleointensities for NWA 7325 for total TRM acquired in paleofields as weak as approximately $0.3 \times 10 = 3 \mu\text{T}$.

Supplementary Figures

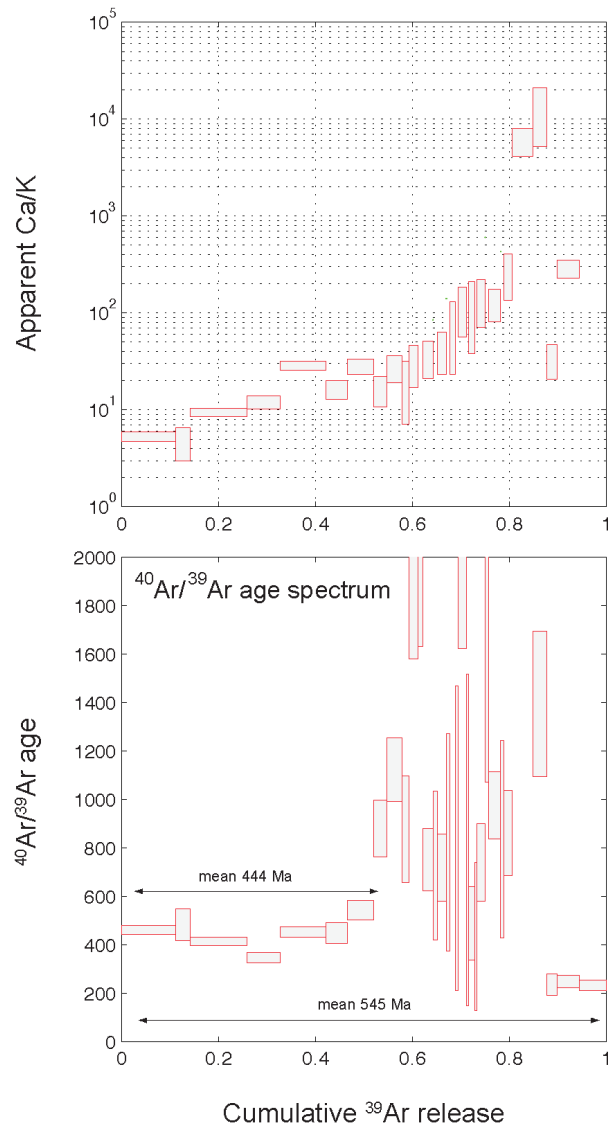


Fig. S1. Ar isotopic analyses of a ~1 mg whole-rock sample of NWA 7325. (Bottom) Apparent $^{40}\text{Ar}/^{39}\text{Ar}$ age release spectrum. Each spectrum is plotted against the cumulative release fraction of ^{39}Ar . Dimensions of boxes indicate $\pm 1\text{-}\sigma$ (vertical) and the fraction of ^{39}Ar released (horizontal). Error-weighted mean ages are labeled and calculated from subsets of data as indicated with arrows. (Top) Corresponding apparent Ca/K ratios inferred from the ratio of released ^{37}Ar to ^{39}Ar .

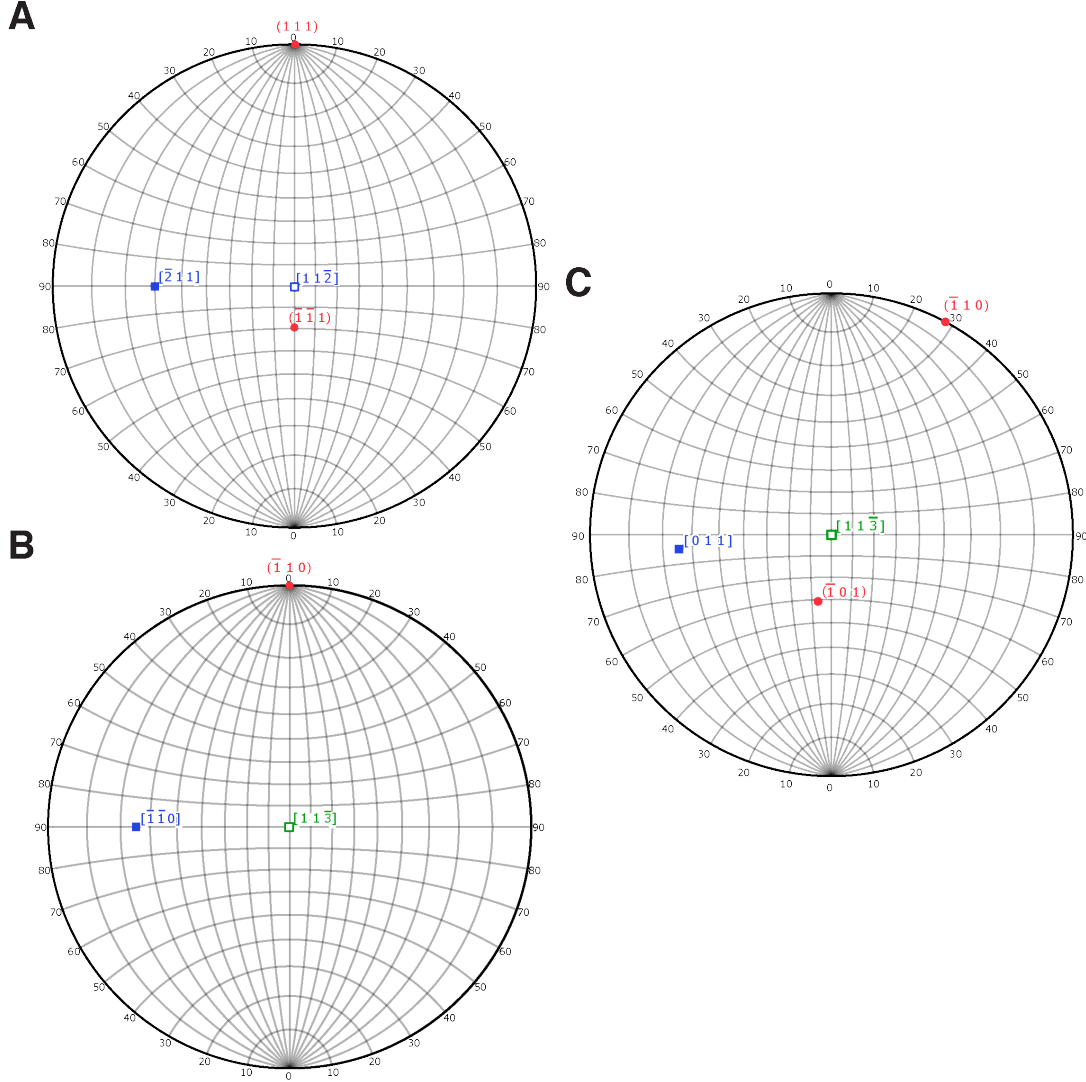


Fig. S2. Stereograms illustrating the possible martensite twin relations observed in Fig. 1H. The martensitic transformation of γ -FeNi to α_2 -FeNi is specified by the Greninger-Troiano relationship (Goldstein and Michael, 2006; Kelly et al., 1990; Morito et al., 2006): $\langle \bar{1}2\bar{1} \rangle_\gamma \sim 2^\circ \parallel \langle \bar{1}\bar{1}0 \rangle_\alpha$ and $\{111\} \parallel \{011\}_\alpha$. Open symbols denote lower hemisphere and closed symbols denote upper hemisphere. (A) Stereogram of γ -FeNi (fcc) viewed along $[11\bar{2}]$ and showing the $[\bar{2}11]$ direction (blue) and the pole to the (111) and $(\bar{1}\bar{1}1)$ planes (red). (B) Stereogram of α_2 -FeNi (bcc) viewed along the $[11\bar{3}]$ zone axis (green) and showing the $[\bar{1}\bar{1}0]$ vector (blue) and the pole to the $(\bar{1}10)$ plane (red). This orientation, which corresponds to one of the two diffraction patterns in Fig. 1H, places the $[\bar{1}\bar{1}0]$ vector (blue) and the pole to $(\bar{1}10)$ (red), nearly coincident with $[\bar{2}11]_\gamma$ and $(111)_\gamma$, respectively in (A). (C) Stereogram of α -FeNi (bcc) viewed along the $[11\bar{3}]$ zone axis (green), but rotated 28° clockwise relative to (B) along $[11\bar{3}]$ in (B). This orientation nearly represents the orientation of the second diffraction pattern in Fig. 1H. In this case, the $[011]$ and $(\bar{1}01)$ vectors plot near $[\bar{2}11]_\gamma$ and $(\bar{1}\bar{1}1)_\gamma$ in (A). However, in the measured selected area electron diffraction pattern (Fig. 1H) the second pattern is not viewed directly down the zone axis. These stereograms illustrate that the measured pattern is consistent with a crystallographic relationship close to the Greninger-Troiano relationship.

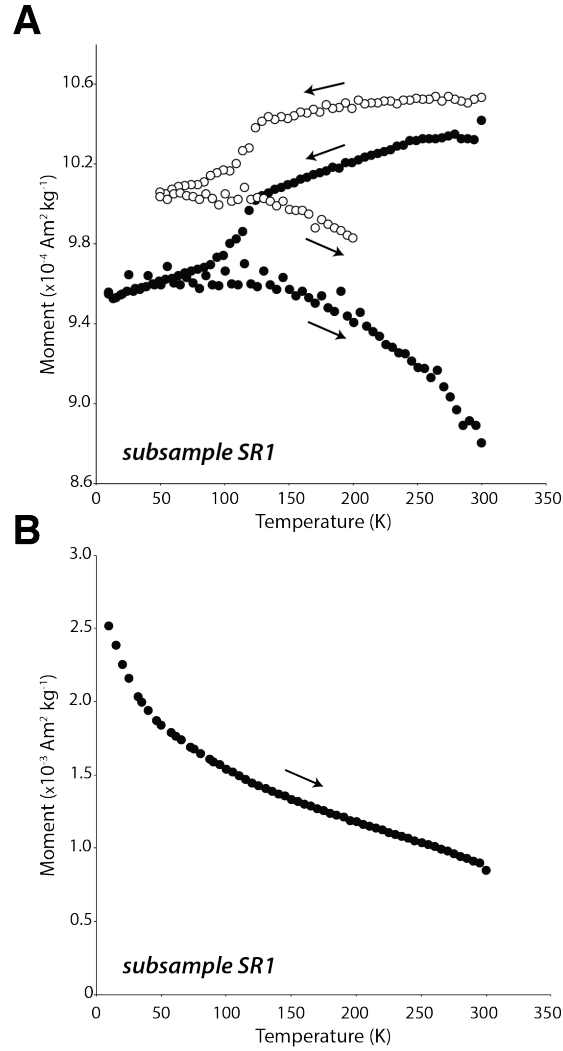


Fig. S3. Low temperature magnetic measurements on fresh NWA 7325 subsample SR1. (A) Room temperature cycling of saturation Irm. Sample was exposed to a 2.5 T at 300 K and cycled in near-zero field conditions down to low temperature and then warmed up again. This experiment was conducted on the same sample twice, with the first experiment cycled down to 10 K (closed symbols) and the second experiment down to 50 K (open symbols). (B) Field cooled (FC) warming experiment. Same subsample was exposed to a 2.5 T while cooling from 300 K to 10 K and then warmed up in near-zero field.

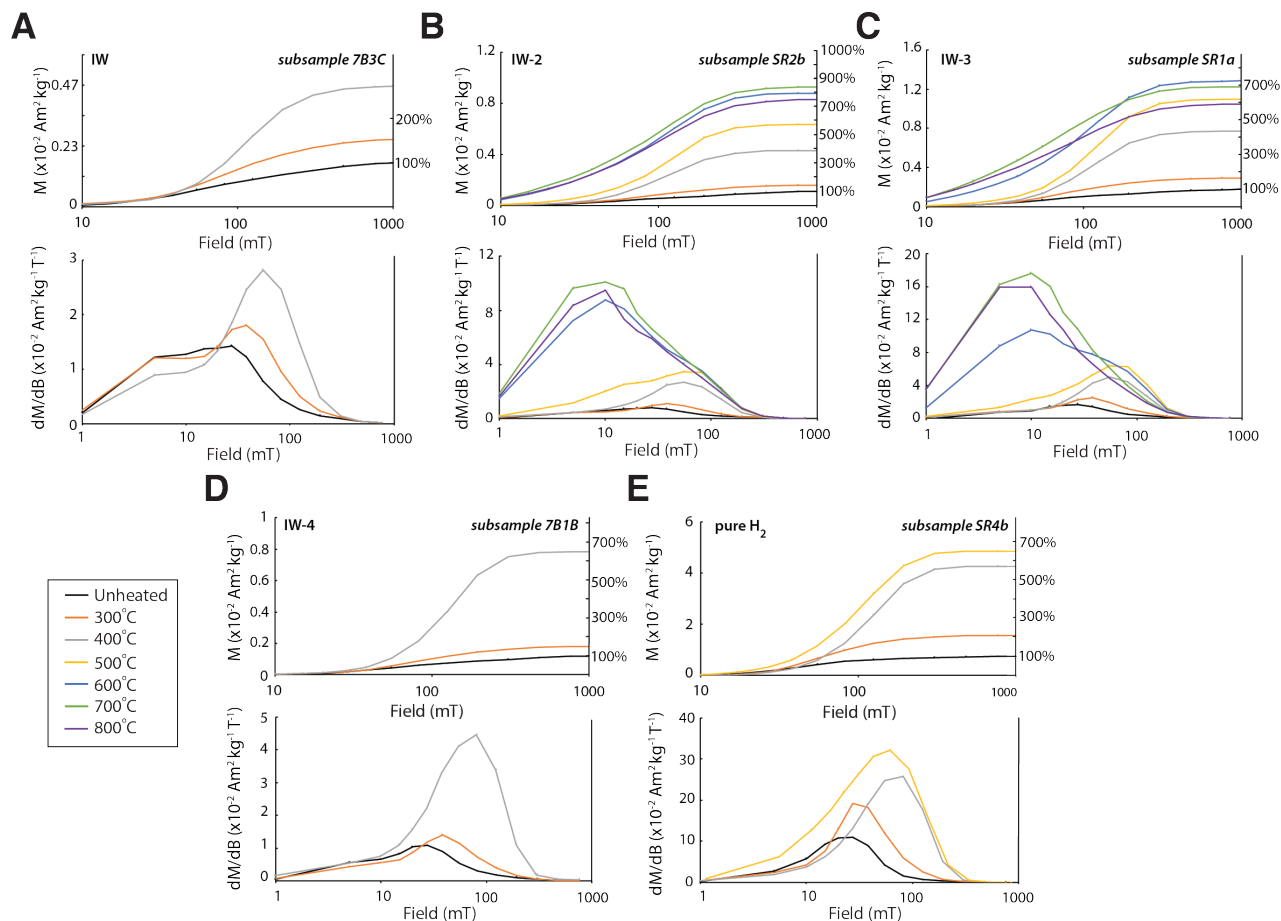


Fig. S4. Thermal alteration tests on NWA 7235. Shown are IRM acquisition curves and their derivatives for heating to various peak temperatures under varying oxygen fugacity conditions. **(A)** Subsample 7B3C (~20 mg estimated weight) in IW conditions. **(B)** Subsample SR2b in IW-2 conditions (8.5 mg). **(C)** Subsample SR1a (44.0 mg) in IW-3 conditions. **(D)** Subsample 7B1B (11.6 mg) in IW-4 conditions. **(E)** Subsample SR4b (7.9 mg) in a near-pure H_2 atmosphere.

Table S1. Analytical details for our $^{40}\text{Ar}/^{39}\text{Ar}$ measurements.

COMPLETE $^{40}\text{Ar}/^{39}\text{Ar}$ INCREMENTAL HEATING RESULTS

#	Temp (°C)	^{40}Ar ± 1σ	^{39}Ar ± 1σ	^{38}Ar ± 1σ	^{37}Ar ± 1σ	^{36}Ar ± 1σ	$^{40}\text{Ar}^*$ (%)	$^{39}\text{Ar}_k$ (%)	$^{38}\text{Ar}_{\text{cos}}$ (%)	$^{38}\text{Ar}_{\text{trap}}$ (%)	$^{36}\text{Ar}_{\text{cos}}$ (%)	$^{36}\text{Ar}_{\text{trap}}$ (%)	Ca/K	$^{40}\text{Ar}/^{39}\text{Ar}$ Age ± 1s (Ma)
NWA7325-B72 whole-rock fragment														
1	446 °C	6.72 ± 0.01	0.302 ± 0.003	0.005 ± 0.0024	0.821 ± 0.007	0.011 ± 0.0084	100.0	99.8	-7.2	39.1	100.3	100.3	5.3	474 ± 17
2	446 °C	1.88 ± 0.01	0.080 ± 0.003	0.001 ± 0.0024	0.194 ± 0.006	0.002 ± 0.0084	100.0	99.8	-0.9	31.9	-0.3	98.2	4.8	495 ± 24
3	496 °C	6.21 ± 0.01	0.316 ± 0.003	0.008 ± 0.0024	1.518 ± 0.010	0.011 ± 0.0084	100.0	99.7	28.3	22.2	13.0	83.4	9.4	424 ± 15
4	496 °C	3.01 ± 0.01	0.186 ± 0.003	0.004 ± 0.0024	1.141 ± 0.009	0.006 ± 0.0084	100.0	99.6	21.9	22.6	10.0	84.8	12.1	356 ± 14
5	546 °C	5.58 ± 0.01	0.258 ± 0.003	0.011 ± 0.0024	3.770 ± 0.015	0.022 ± 0.0084	100.0	99.0	39.7	31.2	12.8	82.6	28.9	464 ± 17
6	546 °C	2.53 ± 0.01	0.118 ± 0.003	0.005 ± 0.0024	0.993 ± 0.009	0.010 ± 0.0084	100.0	99.4	37.2	33.4	11.7	85.8	16.6	459 ± 19
7	597 °C	4.00 ± 0.01	0.151 ± 0.003	0.012 ± 0.0024	2.147 ± 0.012	0.032 ± 0.0084	100.0	99.0	40.6	44.1	9.9	88.3	28.2	555 ± 21
8	595 °C	3.57 ± 0.01	0.075 ± 0.003	0.006 ± 0.0024	0.621 ± 0.007	0.019 ± 0.0084	100.0	99.4	32.4	52.7	6.9	92.2	16.4	898 ± 41
9	645 °C	5.41 ± 0.01	0.083 ± 0.003	0.013 ± 0.0024	1.153 ± 0.009	0.049 ± 0.0084	100.0	99.0	28.0	64.3	5.0	94.4	27.6	1146 ± 47
10	645 °C	1.84 ± 0.01	0.039 ± 0.003	0.005 ± 0.0024	0.384 ± 0.007	0.016 ± 0.0084	100.0	99.3	26.3	63.1	4.8	94.6	19.5	895 ± 62
11	696 °C	7.24 ± 0.01	0.053 ± 0.003	0.019 ± 0.0024	0.856 ± 0.007	0.069 ± 0.0084	100.0	98.9	30.9	65.5	5.4	94.3	31.7	1885 ± 83
12	695 °C	4.70 ± 0.01	0.024 ± 0.003	0.009 ± 0.0024	0.406 ± 0.007	0.032 ± 0.0084	100.0	98.8	31.8	64.7	5.6	94.0	33.1	2328 ± 174
13	748 °C	2.29 ± 0.01	0.059 ± 0.003	0.022 ± 0.0024	1.072 ± 0.009	0.075 ± 0.0084	100.0	98.7	35.9	60.8	6.7	92.9	36.2	769 ± 41
14	745 °C	0.90 ± 0.00	0.024 ± 0.003	0.006 ± 0.0024	0.509 ± 0.007	0.019 ± 0.0084	100.0	98.5	47.3	48.1	10.6	88.7	42.2	743 ± 82
15	798 °C	1.96 ± 0.01	0.053 ± 0.003	0.014 ± 0.0024	1.151 ± 0.010	0.039 ± 0.0084	100.0	98.5	50.6	44.8	12.0	87.2	43.2	736 ± 42
16	794 °C	0.78 ± 0.00	0.018 ± 0.003	0.005 ± 0.0024	0.545 ± 0.008	0.011 ± 0.0084	100.0	97.9	64.9	30.9	20.1	78.6	60.5	841 ± 117
17	845 °C	10.37 ± 0.01	0.035 ± 0.003	0.016 ± 0.0024	1.330 ± 0.010	0.047 ± 0.0084	100.0	97.3	50.4	46.9	11.5	87.8	76.9	2948 ± 141
18	845 °C	0.58 ± 0.00	0.013 ± 0.003	0.005 ± 0.0024	0.660 ± 0.008	0.005 ± 0.0084	100.0	96.5	87.5	9.0	52.4	44.3	101.6	859 ± 162
19	898 °C	6.60 ± 0.01	0.046 ± 0.003	0.240 ± 0.0025	2.741 ± 0.012	0.184 ± 0.0084	100.0	95.9	97.2	2.5	82.0	17.6	120.5	1978 ± 94
20	898 °C	0.52 ± 0.00	0.012 ± 0.003	0.006 ± 0.0024	0.868 ± 0.008	0.005 ± 0.0084	100.0	95.1	91.5	5.7	63.3	32.4	146.8	852 ± 175
21	948 °C	0.81 ± 0.01	0.036 ± 0.003	0.016 ± 0.0024	2.178 ± 0.011	0.017 ± 0.0084	100.0	95.8	88.1	9.0	52.5	44.2	124.9	501 ± 42
22	948 °C	0.31 ± 0.00	0.016 ± 0.003	0.008 ± 0.0024	1.148 ± 0.010	0.006 ± 0.0084	100.0	94.9	94.3	3.0	75.3	19.8	150.2	445 ± 80
23	998 °C	1.77 ± 0.01	0.048 ± 0.003	0.026 ± 0.0024	3.384 ± 0.014	0.025 ± 0.0084	100.0	95.1	91.3	6.3	61.5	34.8	145.4	757 ± 47
24	998 °C	2.49 ± 0.01	0.022 ± 0.003	0.256 ± 0.0025	2.850 ± 0.014	0.176 ± 0.0084	100.0	91.0	99.1	0.8	93.3	6.3	278.5	1771 ± 174
25	1048 °C	3.58 ± 0.01	0.068 ± 0.003	0.034 ± 0.0024	4.275 ± 0.019	0.036 ± 0.0084	100.0	95.7	89.3	8.1	55.5	41.3	128.1	996 ± 46
26	1048 °C	0.88 ± 0.00	0.021 ± 0.003	0.014 ± 0.0024	1.977 ± 0.012	0.009 ± 0.0084	100.0	93.5	98.4	-0.4	97.7	-3.6	197.1	854 ± 107
27	1098 °C	2.20 ± 0.01	0.052 ± 0.003	0.045 ± 0.0024	6.499 ± 0.021	0.036 ± 0.0084	100.0	91.3	96.1	2.3	79.4	15.8	269.7	879 ± 52
28	1198 °C	25.60 ± 0.03	0.355 ± 0.003	2.420 ± 0.0043	348.417 ± 0.924	1.779 ± 0.0089	100.0	31.8	98.6	1.1	86.8	8.0	6049.0	2526 ± 77
29	1245 °C	6.83 ± 0.01	0.435 ± 0.003	3.534 ± 0.0055	515.987 ± 1.677	2.568 ± 0.0094	100.0	17.6	98.8	0.9	88.0	6.6	13178.5	1421 ± 85
30	1248 °C	0.66 ± 0.01	0.063 ± 0.003	0.008 ± 0.0024	1.076 ± 0.010	0.007 ± 0.0084	100.0	98.8	85.8	4.8	65.7	30.2	34.1	243 ± 14
31	1297 °C	1.37 ± 0.01	0.134 ± 0.003	0.126 ± 0.0024	17.845 ± 0.097	0.091 ± 0.0084	100.0	90.7	97.6	1.0	87.5	7.3	288.2	255 ± 11
32	1296 °C	1.58 ± 0.02	0.150 ± 0.003	0.003 ± 0.0024	0.0004 ± 0.0059	0.004 ± 0.0084	100.0	100.0	21.4	22.3	10.5	89.5	0.0045	239 ± 10

Isotope abundances given in 10^{-15} mol (spectrometer sensitivity is $\sim 1.12 \times 10^{-14}$ mols/nA), and corrected for ^{37}Ar and ^{39}Ar decay, half-lives of 35.2 days and 269 years, respectively, and for spectrometer discrimination per atomic mass unit of 1.004535 ± 0.002968 .

Isotope sources calculated using the reactor constants in Renne et al. (1998), assuming $(^{38}\text{Ar}/^{36}\text{Ar})_{\text{cos}} = 1.54$, $(^{38}\text{Ar}/^{36}\text{Ar})_{\text{trap}} = 0.188$, and $(^{40}\text{Ar}/^{36}\text{Ar})_{\text{trap}} = 0$.

No corrections were made for cosmogenic ^{40}Ar .

Ages calculated using the decay constants and standard calibration of Renne et al. (2011) and isotope abundances of Steiger and Jäger (1977) and calculated relative to Hb3gr fluence monitor (1081 Ma). Corrections were made for reactor produced ^{38}Ar and ^{36}Ar in age calculations. J-Value is 0.0134147 ± 0.0005212 .

Average analytical blanks are: $^{40}\text{Ar} = 0.015$; $^{39}\text{Ar} = 0.0001$; $^{38}\text{Ar} = 0.00002$; $^{37}\text{Ar} = 0.0001$; $^{36}\text{Ar} = 0.00007$ (nanoamps).

Temperature was controlled with approximately ± 10 °C precision and ± 10 °C accuracy; each heating duration was 600 seconds.

Table S2. WDS analyses (in units of weight %) of Fe-rich grains in NWA 7325.

Spot #	Occurrence and Description	Si	O	S	Fe	Mg	Al	Cl	Ni	Cr	Ca	Total
1	~10 µm sulfide in plagioclase	0.07	3.12	35.04	58.54	0.08	0.01	0.00	0.14	2.65	0.00	99.65
2	Fe oxide alteration phase in plagioclase	4.53	36.55	0.12	48.66	1.50	1.61	0.00	1.87	0.02	2.21	97.07
3	~50 µm sulfide in diopside	0.02	0.45	34.98	60.23	0.00	0.01	0.00	0.27	2.92	0.00	98.87
3b	~50 µm sulfide in diopside	0.00	0.83	35.48	60.03	0.00	0.00	0.00	0.26	2.91	0.00	99.51
3c	~50 µm sulfide in diopside	0.00	0.30	35.35	60.36	0.02	0.00	0.00	0.23	2.84	0.00	99.10
4a	~15 µm metal grain next to grain #5	0.01	0.34	0.10	86.81	0.00	0.00	0.00	9.86	0.14	0.00	97.26
4b	~15 µm metal grain next to grain #5	0.06	0.42	0.02	87.54	0.00	0.02	0.00	9.15	0.18	0.00	97.39
5a	~100 x 20 µm sulfide grain next to grain #4	0.00	0.40	35.63	58.61	0.02	0.00	0.00	0.20	3.94	0.00	98.80
5b	~100 x 20 µm sulfide grain next to grain #4	0.00	0.62	36.11	58.44	0.00	0.01	0.00	0.23	3.95	0.00	99.37
5c	~100 x 20 µm sulfide grain next to grain #4	0.03	0.55	35.56	58.78	0.00	0.00	0.00	0.27	3.91	0.00	99.10
6a	Cr-metal assemblage in forsterite (Fig. 1B)	0.10	0.00	0.00	71.44	0.10	0.01	0.00	7.87	17.47	0.00	96.99
6b	Cr-metal assemblage in forsterite (Fig. 1B)	1.04	1.71	0.00	69.70	0.72	0.10	0.00	7.83	16.92	0.00	98.03
6c	Cr-metal assemblage in forsterite (Fig. 1B)	0.29	0.47	0.02	71.18	0.38	0.01	0.00	8.40	17.07	0.00	97.81
6d	Cr-metal assemblage in forsterite (Fig. 1B)	0.13	0.00	0.00	72.40	0.13	0.00	0.00	8.23	17.43	0.00	98.33
6e	Cr-metal assemblage in forsterite (Fig. 1B)	0.23	0.00	0.00	71.32	0.26	0.00	0.00	8.21	17.26	0.00	97.28
7a	~3 µm metal bordering grain #8	0.10	0.58	0.05	83.79	0.03	0.00	0.00	10.32	0.14	0.00	95.01
7b	~3 µm metal bordering grain #8	0.18	0.55	0.05	83.91	0.05	0.00	0.00	9.62	0.12	0.00	94.48
8a	~10 µm sulfide bordering grain #7	0.04	0.65	35.32	59.58	0.05	0.00	0.00	0.23	2.34	0.00	98.21
8b	~10 µm sulfide bordering grain #7	0.04	0.74	35.19	59.08	0.00	0.01	0.00	0.29	2.68	0.00	98.03
8c	~10 µm sulfide bordering grain #7	0.20	0.68	34.93	59.31	0.06	0.02	0.00	0.15	2.34	0.00	97.69
9	Chromite	0.68	29.86	1.20	16.91	4.32	0.22	0.00	0.01	47.12	0.64	100.95
10a	~3 µm metal inclusion in sulfide grain #11 (Fig. 1C)	0.03	0.52	0.01	92.55	0.04	0.01	0.00	5.54	0.06	0.00	98.75
10b	~3 µm metal inclusion in sulfide grain #11 (Fig. 1C)	0.08	0.53	0.00	90.87	0.00	0.03	0.00	5.94	0.07	0.00	97.52
11a	~50 µm sulfide enclosing grain #10 (Fig. 1C)	0.01	0.47	35.58	60.61	0.00	0.00	0.00	0.13	2.66	0.00	99.46
11b	~50 µm sulfide enclosing grain #10 (Fig. 1C)	0.01	0.57	35.49	60.53	0.01	0.00	0.00	0.14	2.74	0.00	99.50
11c	~50 µm sulfide enclosing grain #10 (Fig. 1C)	0.03	0.58	35.30	60.63	0.00	0.01	0.00	0.12	2.63	0.00	99.32
12	~2 µm secondary oxide in sulfide grain #11 (Fig. 1C)	2.24	31.61	1.91	51.09	0.80	0.30	1.30	6.00	0.35	1.13	96.73

Note: The first column contains the number of the spot where the measurement was taken; spots from different locations in the same grains are labeled with the same number followed by different letters. The second column describes the petrographic setting of each measured grain. The third through twelfth columns contain the elemental abundances in weight percent for Si, O, S, Fe, Mg, Al, Cl, Ni, Cr, and Ca, respectively. The thirteenth column contains the sum (in percent) of the measured elemental abundances.

Table S3. Hysteresis and back-field IRM for NWA 7325 and paired stone NWA 8268.

Sample	Pre-treatment	Mass (mg)	M_{rs} ($\text{Am}^2 \text{kg}^{-1}$)	M_s ($\text{Am}^2 \text{kg}^{-1}$)	M_{rs}/M_s	B_{cr} (mT)	B_c (mT)	B_{cr}/B_c
SR3	Unheated	46	9.77×10^{-4}	0.0339	0.029	48.2	7.78	6.20
SR1	Unheated	60	1.22×10^{-3}	0.0545	0.022	41.9	6.38	6.57
JG2	Unheated	905	1.58×10^{-3}	0.0802	0.020	51.4	7.63	6.74
7B3C	400°C IW-0	15*	7.22×10^{-3}	0.0965	0.075	67.1	15.2	4.43
SR1a	800°C IW-3	44	0.0139	0.368	0.038	27.0	4.09	6.60

Notes: The first column gives the subsample name, the second column lists whether and how the sample experience laboratory heating prior to the measurements listed here, the third column gives the mass, the fourth column gives the saturation remanent magnetization (M_{rs}), the fifth column gives the saturation magnetization (M_s), the sixth column gives the ratio M_{rs} to M_s , the seventh column gives the coercivity of remanence (B_{cr}), the eighth column gives the coercivity (B_c), and the ninth column gives the ratio of B_{cr} to B_c . Subsamples SR3, 7B3C and SR1a were measured with an alternating gradient force magnetometer in the Rutgers Paleomagnetism Laboratory, SR1 was measured with a vibrating sample magnetometer at the Institute for Rock Magnetism at the University of Minnesota, and JG2 was measured with a vibrating sample magnetometer at CEREGE, Aix-en-Provence. All subsamples were drawn from NWA 7325 except for JG2, which was drawn from NWA 8268. SR1a is a subsample of SR1.

*Estimated weight

Table S4. NRM components as identified by principal components analysis (PCA).

Sample	Mass (mg)	Component	Range (mT/°C)	<i>N</i>	Anchored?	Dec. (°)	Inc. (°)	MAD (°)
B71	84.0	LC	NRM-16 mT	17	N	250.5	3.3	20.7
		HC range	16-85 mT	30	Y	145.5	7.1	46.8
B72	70.0	LC ¹	NRM- <52 mT	2	N	263.9	0.0	-
		HC range	52-85 mT	18	Y	275.2	-59.0	28.6
B73	107	LC	NRM-5 mT	9	N	271.5	-2.1	5.9
		MC	5-20.5 mT	32	N	116.5	-10.4	35.8
		HC range	20.5-150 mT	46	Y	172.1	-24.7	29.3
B74	73.7	LT ²	NRM-165°C	13	N	267.2	-8.0	13.8
		HT range	165-515°C	16	Y	118.0	33.4	36.7
B75	62.5	LC	NRM-4 mT	7	N	267.5	16.8	10.2
		MT ²	4 mT-378°C	16	N	113.6	-22.1	26.4
		HT range	378-515°C	7	Y	1.1	32.0	23.8
B76	67.6	LT	NRM-340°C	6	N	252.8	-37.5	13.6
		HT range ³	340-800°C	20	Y	262.4	-35.7	29.7
B77	82.4	LT	NRM-340°C	7	N	315.5	-68.0	35.5
		HT range ³	340-800°C	20	Y	291.3	-32.6	30.2
B78	69.8	LT	NRM-300°C	6	N	272.1	20.1	15.9
		HT range	300-800°C	20	Y	287.5	-8.4	24.7
B79	73.2	LT	NRM-300°C	6	N	259.7	-9.7	20.6
		HT range	300-800°C	20	Y	256.1	19.6	45.4

Notes: The first column gives the subsample name, the second column gives its mass, the third column lists the component or magnetization name, the fourth column lists the range in mT or °C, the fifth column lists the number of points used in the PCA fit, the sixth column specifies whether the fit was anchored to the origin, the seventh column lists the declination, the eighth column lists the inclination, and the ninth column lists the maximum angular deviation (MAD).

¹Two-point fit because first AF step was 52 mT.

²Includes repeat NRM measurement between final (5 mT) AF demagnetization step and before first (50°C) thermal demagnetization step.

³The NRMs of these samples were not completely thermally demagnetized (reached peak a heating temperature of 400°C) prior to giving them a 400°C pTRM. However, this pTRM was essentially completely removed by subsequent thermal demagnetization to 400°C as indicated by the remanence having nearly returned to that just prior to application of the pTRM. Therefore, the HT range for these samples was fit using thermal demagnetization steps following the pTRM application for temperatures of 400°C and above.

Table S5. Summary of paleointensities for NWA 7325.

Sample	Type	LC/LT (μT)	LC/LT Corrected (μT)	MC/MT (μT)	MC/MT Corrected (μT)	HC/HT (μT)	HT Corrected (μT)
B71	ARM 200 mT AF, 200 μT bias	58 ± 24	58 ± 24	-	-	1.5 ± 7.1	1.5 ± 7.1
	IRM	41 ± 18	41 ± 18	-	-	0.68 ± 5.19	0.68 ± 5.19
B73	ARM 200 mT AF, 400 μT bias	190 ± 36	190 ± 36	11 ± 4	11 ± 4	1.8 ± 3.5	1.8 ± 3.5
	IRM	140 ± 27	140 ± 27	6.2 ± 2.4	6.2 ± 2.4	1.1 ± 2.0	1.1 ± 2.0
B74B ^{1,2}	pTRM 515°C, 50 μT	52 ± 42	310 ± 250	-	-	5.7 ± 5.6	34 ± 34
B74S ^{1,2}	pTRM 515°C, 50 μT	68 ± 44	410 ± 270	-	-	6.4 ± 4.5	38 ± 27
B75 ²	pTRM 515°C, 50 μT	59 ± 12	350 ± 72	-	-	7.6 ± 4.3	46 ± 26
B76	pTRM 400°C, 30 μT	11 ± 2	33 ± 6	-	-	7.4 ± 16.8	22 ± 50
B77	pTRM 400°C, 30 μT	3.1 ± 3.2	9.3 ± 9.6	-	-	16 ± 26	48 ± 78
B78	TRM 800°C, 30 μT	3.1 ± 2.0	31 ± 20	-	-	0.37 ± 0.31	3.7 ± 3.1
B79	TRM 800°C, 30 μT	0.64 ± 0.37	64 ± 37	-	-	0.12 ± 0.27	1.2 ± 2.7
Mean ³			23 ± 5		7.5 ± 2.1		1.7 ± 1.4

Notes: The first column lists the subsample name, the second column lists the paleointensity method, the third and fourth columns give the raw and alteration-corrected paleointensity estimates for the LC/LT component, the fifth and sixth columns give the raw and alteration-corrected paleointensity estimates for MC/MT components, and the seventh and eighth columns give the raw and alteration-corrected paleointensity estimates for HC/HT range. Paleointensities were not measured for sample B72. Quoted uncertainties only represent that associated with the linear regression and do not take into account systematic uncertainties associated with the unknown values of f' and a . They were calculated using a two-tailed Student's t -test (Weisberg, 1985) on the slope estimates for the NRM lost versus ARM lost/IRM lost/TRM lost data. Alteration-corrected paleointensities computed by multiplying the raw values by the following factors: $\times 6$ for B74B, B74S, and B75, $\times 3$ for B76 and B77, and $\times 10$ for B78 and B79. See Section 2.2 and main text Section 3.2.

¹Samples B74B and B74S are subsamples of the parent sample B74. The NRM of B74 was demagnetized as a single sample, while thermal demagnetization of pTRM was measured separately for the daughter subsamples B74B and B74S. The paleointensities for these subsamples were estimated by normalizing the NRM of B74 by the respective subsample masses.

²For these samples, the lowest temperature step used to thermally demagnetize their laboratory pTRMs was 353°C. Therefore, their LC/LT paleointensities can only be computed over the range 0 to 5 mT and the paleointensity for the MT component of B75 cannot be estimated.

³Mean values and associated uncertainty of the means were calculated using all experiments on each subsample individually weighted by the inverse of the square of the uncertainties (Taylor, 1997). Samples B74B, B74S, B75 were excluded from the LC/LT means and B74B, B74S, B75, B76 and B77 were excluded from the HC/HT means due to their high uncertainties. If these subsamples were included, the mean LC/LT and HC/HT values would become 36 ± 5 and 2.0 ± 1.4 μT , respectively.

Table S6. ARM paleointensity fidelity test for NWA 7325.

Sample	ARM Bias Field (μT)	TRM-Equivalent Field (μT)	Recovered Field (μT)	Uncertainty (μT)	Difference (%)	Error (%)
B71	10	7.5	3.7	7.3	51	97
B71	15	11	7.2	5.9	35	54
B71	20	15.0	13.5	9.0	10	60
B73	4	3.0	-2.2	3.3	173	110
B73	7	5.2	4.8	6.1	8	117
B73	10	7.5	6.8	2.8	9	37

Note: The first column gives the subsample name, the second column gives the DC bias field used to create the ARM ("artificial NRM"), the third column gives the equivalent paleofield intensity for a TRM, the fourth column gives the field estimate from the ARM paleointensity experiment, the fifth column the 95% confidence interval calculated using a two-tailed Student's *t*-test (Weisberg, 1985) for the slope estimates from the artificial NRM lost versus ARM lost data, the sixth column gives the difference metric, and the seventh column gives the error metric (see Section 3.1).

Supplementary References

- Gattacceca, J., Rochette, P., 2004. Toward a robust normalized magnetic paleointensity method applied to meteorites. *Earth Planet. Sci. Lett.* 227, 377-393.
- Gattacceca, J., Suavet, C., Rochette, P., Weiss, B.P., Winklhofer, M., Uehara, M., Friedrich, J.M., 2014. Metal phases in ordinary chondrites: Magnetic hysteresis properties and implications for thermal history. *Meteorit. Planet. Sci.* 49, 652-676.
- Goldstein, J.I., Michael, J.R., 2006. The formation of plessite in meteoritic metal. *Meteorit. Planet. Sci.* 41, 553-570.
- Ito, M., Ganguly, J., 2005. Closure temperatures of the short-lived decay systems, Be-B in melilite and Al-Mg in anorthite: Implications for the chronology of CAIs and early solar system events. *Lunar Planet. Sci. Conf. XXXVI*, abstract #1552.
- Ito, M., Ganguly, J., 2009. Magnesium diffusion in minerals in CAIs: New experimental data for melilites and implications for the Al-Mg chronometer and thermal history of CAIs. *Lunar Planet. Sci. Conf. XL*, abstract #1753.
- Jull, A.J.T., 2006. Terrestrial ages of meteorites, in: Lauretta, D.S., McSween, H.Y. (Eds.), *Meteorites and the Early Solar System II*. University of Arizona Press, Tucson, pp. 889-905.
- Kelly, P.M., Jostons, A., Blake, R.G., 1990. The orientation relationship between lath martensite and austenite in low carbon low alloy steels. *Acta Metall. Mater.* 38, 1075-1081.
- Koefoed, P., Amelin, Y., Yin, Q.-Z., Wimpenny, J., Sanborn, M.E., Iizuka, T., Irving, A.J., 2016. U-Pb and Al-Mg systematics of the ungrouped achondrite Northwest Africa 7325. *Geochim. Cosmochim. Acta* 183, 31-45.
- LaTourrette, T., Wasserburg, G.J., 1998. Mg diffusion in anorthite: Implications for the formation of early solar system planetesimals. *Earth Planet. Sci. Lett.* 158, 91-108.
- Morito, S., Huang, X., Furuhashi, T., Maki, T., Hansen, N., 2006. The morphology and crystallography of lath martensite in alloy steels. *Acta Mater.* 54, 5323-5331.
- Shuster, D.L., Cassata, W.S., 2015. Paleotemperatures at the lunar surfaces from open system behavior of cosmogenic ^{38}Ar and radiogenic ^{40}Ar . *Geochim. Cosmochim. Acta* 155, 154-171.
- Taylor, J.R., 1997. *An Introduction to Error Analysis: The Study of Uncertainties in Physical Measurements*. University of Science Books, Sausalito, California.
- Tikoo, S.M., Weiss, B.P., Buz, J., Lima, E.A., Shea, E.K., Melo, G., Grove, T.L., 2012. Magnetic fidelity of lunar samples and implications for an ancient core dynamo. *Earth Planet. Sci. Lett.* 337-338, 93-103.
- Tikoo, S.M., Weiss, B.P., Cassata, W.S., Shuster, D.L., Gattacceca, J., Lima, E.A., Suavet, C., Nimmo, F., Fuller, M., 2014. Decline of the lunar core dynamo. *Earth Planet. Sci. Lett.* 404, 89-97.
- Van Orman, J.A., Cherniak, D.J., Kita, N.T., 2014. Magnesium diffusion in plagioclase: Dependence on composition, and implications for thermal resetting of the ^{26}Al - ^{26}Mg early solar system chronometer. *Earth Planet. Sci. Lett.* 384, 79-88.
- Weber, I., Morlok, A., Bischoff, A., Hiesinger, H., Ward, D., Joy, K.H., Crowther, S.A., Jasterzebski, N.D., Gilmour, J.D., Clay, P.L., Wogelius, R.A., Greenwood, R.C., Franchi, I.A., Münker, C., 2016. Cosmochemical and spectroscopic properties of Northwest Africa 7325—A consortium study. *Meteorit. Planet. Sci.* 51, 3-30.
- Weisberg, S., 1985. *Applied Linear Regression*. John Wiley & Sons, New York.
- Weiss, B.P., Tikoo, S.M., 2014. The lunar dynamo *Science* 346, 1246753, DOI: 10.1126/science.1246753.